






Simultaneous T_2 and T_2^* mapping of multiple sclerosis lesions with radial RARE-EPI

Carl J. J. Herrmann^{1,2}  | Antje Els¹ | Laura Boehmert¹  | Joao Periquito¹  |
Thomas Wilhelm Eigentler^{1,3}  | Jason M. Millward¹ | Sonia Waiczies¹  |
Joseph Kuchling^{4,5,6} | Friedemann Paul^{4,5,6} | Thoralf Niendorf^{1,4}

¹Berlin Ultrahigh Field Facility (B.U.F.F.), Max Delbrück Center for Molecular Medicine in the Helmholtz Association, Berlin, Germany

²Department of Physics, Humboldt University of Berlin, Berlin, Germany

³Chair of Medical Engineering, Technical University of Berlin, Berlin, Germany

⁴Experimental and Clinical Research Center, a joint cooperation between the Charité Medical Faculty and the Max Delbrück Center for Molecular Medicine, Berlin, Germany

⁵NeuroCure Clinical Research Center, Charité-Universitätsmedizin, Berlin, Germany

⁶Department of Neurology, Charité-Universitätsmedizin, Berlin, Germany

Correspondence

Thoralf Niendorf, Berlin Ultrahigh Field Facility (B.U.F.F.), Max Delbrück Center for Molecular Medicine in the Helmholtz Association, Robert-Rössle-Strasse 10, 13125 Berlin, Germany.
Email: thoralf.niendorf@mdc-berlin.de

Funding information

European Research Council (ERC) under the European Union's Horizon 2020 research and innovation program, Grant/Award Number: 743077 (ThermalMR)

Purpose: The characteristic MRI features of multiple sclerosis (MS) lesions make it conceptually appealing to pursue parametric mapping techniques that support simultaneous generation of quantitative maps of 2 or more MR contrast mechanisms. We present a modular rapid acquisition with relaxation enhancement (RARE)-EPI hybrid that facilitates simultaneous T_2 and T_2^* mapping (2in1-RARE-EPI).

Methods: In 2in1-RARE-EPI the first echoes in the echo train are acquired with a RARE module, later echoes are acquired with an EPI module. To define the fraction of echoes covered by the RARE and EPI module, an error analysis of T_2 and T_2^* was conducted with Monte Carlo simulations. Radial k-space (under)sampling was implemented for acceleration ($R = 2$). The feasibility of 2in1-RARE-EPI for simultaneous T_2 and T_2^* mapping was examined in a phantom study mimicking T_2 and T_2^* relaxation times of the brain. For validation, 2in1-RARE-EPI was benchmarked versus multi spin-echo (MSE) and multi gradient-echo (MGRE) techniques. The clinical applicability of 2in1-RARE-EPI was demonstrated in healthy subjects and MS patients.

Results: There was a good agreement between T_2/T_2^* values derived from 2in1-RARE-EPI and T_2/T_2^* reference values obtained from MSE and MGRE in both phantoms and healthy subjects. In patients, MS lesions in T_2 and T_2^* maps deduced from 2in1-RARE-EPI could be just as clearly delineated as in reference maps calculated from MSE/MGRE.

Conclusion: This work demonstrates the feasibility of radially (under)sampled 2in1-RARE-EPI for simultaneous T_2 and T_2^* mapping in MS patients.

This is an open access article under the terms of the Creative Commons Attribution-NonCommercial License, which permits use, distribution and reproduction in any medium, provided the original work is properly cited and is not used for commercial purposes.

© 2021 The Authors. *Magnetic Resonance in Medicine* published by Wiley Periodicals LLC on behalf of International Society for Magnetic Resonance in Medicine

KEYWORDS

brain, EPI, MRI, multiple sclerosis, parametric mapping, radial k-space sampling, RARE, transversal relaxation time

1 | INTRODUCTION

Multiple sclerosis (MS) is the most common chronic inflammatory demyelinating disease of the central nervous system.^{1,2} The pathological hallmark of MS is the accumulation of demyelinating lesions in the grey and white matter of the brain.^{3,4} MRI is an indispensable tool for the diagnosis and monitoring of MS. It is used for tracking MS disease activity, for prognostic evaluation, and for monitoring the efficacy and safety of disease-modifying treatments.⁵⁻¹¹ MRI findings have led to a better understanding of the underlying pathophysiology of the disease.^{12,13} Distinct lesion morphology and anatomic distribution obtained from modern MRI techniques allows differentiation between MS and other neuroinflammatory diseases.¹³⁻¹⁶ MRI protocols tailored for MS diagnosis and disease progression monitoring incorporate multiple MRI contrasts including T_1 , DWI, T_2 , FLAIR, and T_2^* .¹⁷ Harmonization initiatives have provided consensus reports for MRI in MS, moving toward standardization and dissemination of protocols that facilitate clinical translation and comparison of data across sites.¹⁸⁻²²

T_2 -weighted imaging is well established and frequently used for identification of white matter (WM) lesions, which have a hyperintense appearance.^{5,23} Although being an important diagnostic criterion for MS,²⁴ the WM lesion load correlates only weakly with clinical disability because of its lack of specificity for lesion severity and the underlying pathophysiology.^{5,23,25} This observation has triggered explorations into parametric mapping of the transverse relaxation time T_2 . T_2 prolongation was observed for normal appearing white matter²⁶⁻²⁹ and could also be indicative of early MS.³⁰ T_2 prolongations in diffusely abnormal white matter,²⁶ as well as deep gray matter,³¹ were reported as an enhanced correlate for clinical disability, which is superior to the correlation with the focal WM lesion load. For T_2 mapping, multi spin-echo (MSE) techniques are most widely used. MSE techniques require long TRs to promote SNR and to mitigate T_1 relaxation effects. This results in long scan times, increases the propensity to bulk motion, and might induce slice misregistration in sequential protocols, which constrains the clinical applicability of T_2 mapping. To overcome the scan time requirements, T_2 mapping strategies that reduce TR³²⁻³⁴ or take advantage of undersampling or acceleration strategies³⁵⁻³⁷ have been implemented.

T_2^* -weighted imaging has become increasingly important in MS. The central vein sign^{5,13,16,38} and rim-like paramagnetic phase changes³⁹ in T_2^* -weighted MRI are considered to be disease-specific imaging markers for MS lesions. T_2^*

is sensitive to iron deposition within lesion formations,^{40,41} which may relate to disease duration, activity, and severity.⁴²⁻⁴⁴ Furthermore, T_2^* was reported to reflect brain tissue changes in patients with minor deficits and early MS, and therefore, may become a tool to assess the development of MS already at an early stage.^{30,45} T_2^* mapping can differentiate new enhancing from non-enhancing MS lesions without gadolinium contrast agents, which helps avoid the risks of repeated administration of these agents.⁴⁶⁻⁴⁸ Multi gradient-recalled echo (MGRE)-based techniques are commonly used for T_2^* mapping. These techniques use low flip angles for RF excitation that permit short TRs and facilitate clinically acceptable scan times.

Given the characteristic MRI features of MS lesions, it is conceptually appealing to pursue techniques that support simultaneous generation of quantitative maps of multiple MR contrasts.^{32,49-60} Dual contrast techniques offer substantial scan time reduction, eliminate the risk for slice misregistration, improve the immunity to bulk motion, and boost clinical use. The current study presents a modular rapid acquisition with relaxation enhancement (RARE)-EPI hybrid, which is a combined acquisition technique variant.⁶¹ It facilitates simultaneous T_2 and T_2^* mapping in a single radially (under) sampled scan (2in1-RARE-EPI). To evaluate and define the fraction of echoes covered by the RARE module and the EPI module, an error analysis of T_2 and T_2^* was conducted with Monte Carlo simulations. The feasibility of 2in1-RARE-EPI for simultaneous T_2 and T_2^* mapping was examined in phantoms mimicking the T_2 and T_2^* relaxation times of brain tissue. For validation of T_2 and T_2^* mapping, 2in1-RARE-EPI was benchmarked against conventional MSE and MGRE techniques. As a precursor to broader clinical studies, the clinical applicability of 2in1-RARE-EPI was demonstrated in an in vivo feasibility study with healthy subjects and MS patients.

2 | METHODS

2.1 | RARE-EPI hybrid

The proposed 2in1-RARE-EPI is a combined acquisition technique variant based on a RARE-EPI hybrid^{62,63} In RARE-EPI, the first echoes in the echo train are acquired with a RARE module. Later echoes are acquired with an EPI module. The combined acquisition technique factor $\lambda = N_{\text{RARE}} * N_{\text{RARE}} + N_{\text{EPI}}^{-1}$ indicates the fraction of RARE echoes in the echo train, where N_{RARE} and N_{EPI} denote the number of echoes acquired in the RARE and EPI modules, respectively. We implemented a radial k-space data sampling

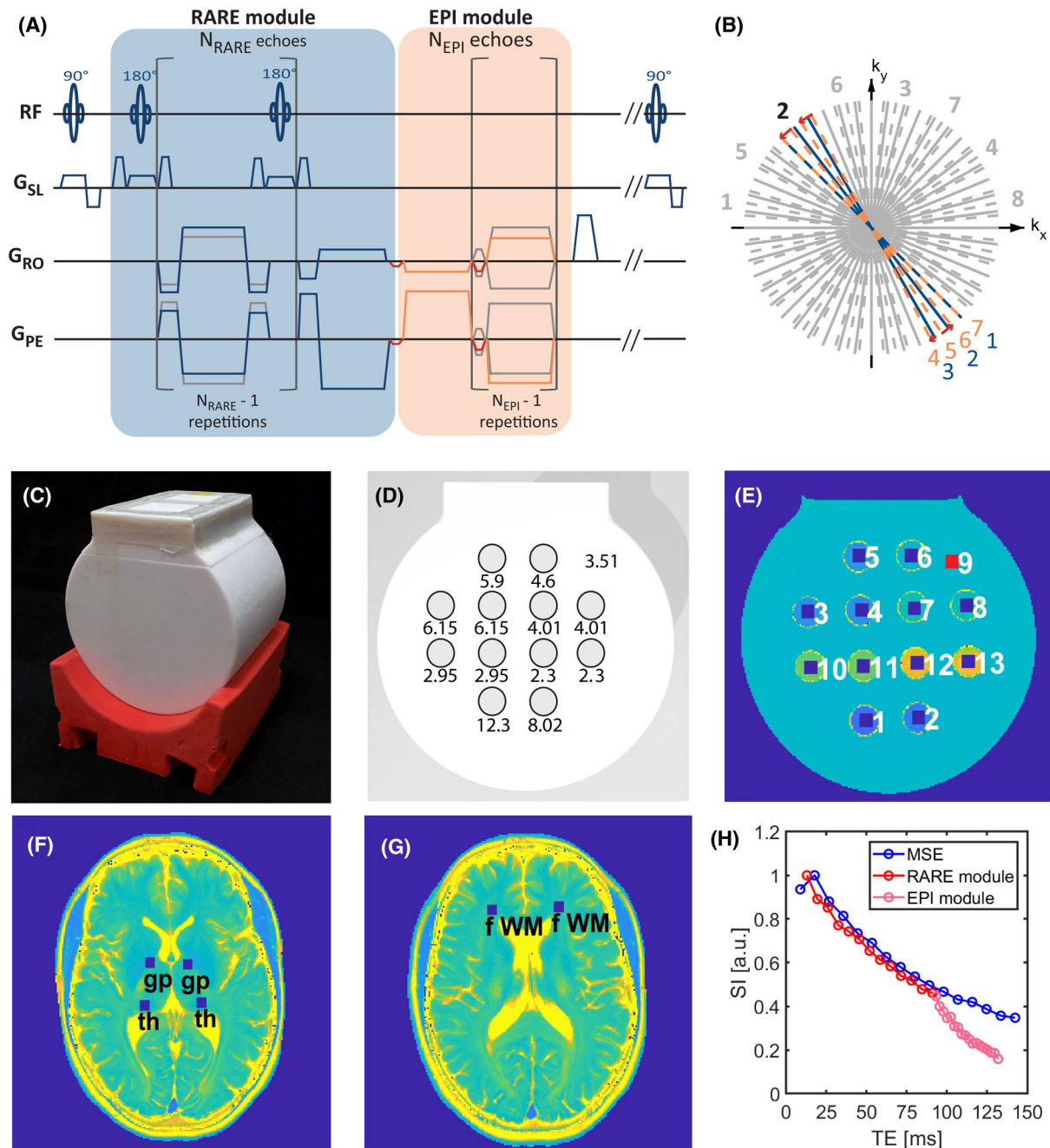


FIGURE 1 (A) Pulse sequence diagram of the radially sampled 2in1-RARE-EPI hybrid. The acquisition of the MR signal with the RARE module (highlighted in light blue) is followed by an acquisition with the EPI module (highlighted in light orange). The first echo in the RARE module is discarded from the acquisition. The EPI module consists of a train of gradient-recalled echoes with bi-polar acquisition, where small blip gradients (marked in red) promote the transition from 1 spoke to the next. (B) Schematic k-space trajectory depicting the illustrative case that 3 RARE and 4 EPI echoes ($\lambda \approx 0.43$) are acquired in the respective modules using 8 shots. The view angles of all RARE echoes (solid lines) and all EPI echoes (dashed lines) are equally distributed. To mitigate motion artefacts in the TE images, the acquisition of k-space segments is equally distributed over the full π radians of k-space within cycles of 4 shots, as denoted by the grey numbers. Within each segment the RARE echoes and EPI echoes are acquired in sequential order, but in reversed directions, as denoted for example, for the second shot by the blue and orange numbers, respectively. The phantom (C) consisted of a 3D printed casing with integrated tube holders. (D) Schematic cross section of the phantom showing the tubes labelled with corresponding iron concentrations used in the phantom studies (iron concentration outside the tubes = $3.51 \mu\text{g Fe/mL}$). The ROIs (size: 9×9 pixels) used for further analysis of the phantom study are depicted in (E). Twelve ROIs are located within the tubes (blue squares), although 1 ROI is located within the body of the phantom (red square). The ROIs (size: 7×7 pixels) used for the scatter and BA plot analysis of the in vivo study involving healthy subjects were placed within the left and right globus pallidus and thalamus (F) and frontal white matter (G). (H) Exemplary signal decay derived from a central voxel of an ROI located in the left globus pallidus. Data were obtained with MSE and 2in1-RARE-EPI. The signal decay is normalized to 1 with respect to the second TE

scheme to facilitate acceleration via k-space undersampling. The pulse sequence diagram and k-space trajectory are depicted in Figure 1A,B. To allow flexible view ordering of the RARE echoes, magnetization is completely rephased before the refocusing RF pulses. In the RARE module, the first spin echo is discarded from the data acquisition. The RARE module is followed by an EPI module, consisting of a train of gradient-recalled echoes with small blip gradients promoting the transition from 1 spoke to the next. The view angles of all RARE and all EPI spokes are equally distributed over the whole π -radian in k-space. To reduce the propensity of the individual TE images to bulk motion, the acquisition of k-space segments is equally distributed over the whole π radians of k-space in cycles of 4 shots. This approach mitigates the grouping of motion-induced errors in k-space.⁶⁴ Within k-space segments, the spokes were acquired sequentially, where the EPI spokes were collected in reversed order with respect to the RARE spokes. For T_2 and T_2^* mapping, images reconstructed from the echoes acquired at the specific TEs were used.

2.2 | Monte Carlo simulations

Because the MR signal undergoes T_2 -decay in the RARE echo train, the SNR left for T_2^* mapping using the EPI echo train is governed by the duration of the RARE module and the T_2 of the tissues under investigation. Therefore, it is reasonable to keep the duration of the RARE module short. Conversely, the sampling of the T_2 decay over a broader time range is desirable to permit accurate estimation of long T_2 values. Similar considerations apply for the T_2^* decay within the EPI echo train. Based on these considerations, Monte Carlo simulations were performed to determine the number of echoes, N_{RARE} and N_{EPI} , which minimize the error in the T_2 and T_2^* estimation. Synthetic data were generated using a mono-exponential decay as a simple model of the MR signal:

$$s_i = \begin{cases} M_0 \cdot \exp\left(-\frac{i \cdot ESP_{\text{RARE}}}{T_2}\right), & 1 \leq i \leq N_{\text{RARE}} \\ s_{N_{\text{RARE}}} \cdot \exp\left(-\frac{i - N_{\text{RARE}} \cdot ESP_{\text{EPI}}}{T_2^*}\right), & N_{\text{RARE}} < i \leq ETL \end{cases} \quad (1)$$

Here, M_0 denotes the initial transverse magnetization, which was set to 1. The echo spacings used in the RARE and EPI module are denoted as ESP_{RARE} and ESP_{EPI} , whereas N_{RARE} and N_{EPI} denote the number of RARE and EPI echoes within the modules. The variable i represents the echo count of the echo train.

For white and gray matter, the literature reports the following T_2 and T_2^* values obtained at 3.0 T: white matter: $T_2 = 70\text{--}90$ ms^{30,65} and $T_2^* = 50\text{--}60$ ms^{30,65}; gray matter: $T_2 = 100\text{--}110$ ms^{66,67} and $T_2^* = 50\text{--}70$ ms.^{67,68} To cover this range,

our simulations used $T_2^* = 30\text{--}70$ ms (10 ms increments) and $T_2 = 70\text{--}110$ ms (20 ms increments).

In a loop of 30,000 repetitions, Rician noise was added to the synthetic data samples according to:

$$s_{\varepsilon} i = \left| s_i + \frac{s_i}{\text{SNR}} \cdot \varepsilon \right|, \varepsilon = N(0, 1), \quad (2)$$

resulting in SNRs of 20 to 70. T_2 and T_2^* were estimated for each repetition using a linear least-square-fit of $\ln(s_{\varepsilon}(i))$. The error in T_2 and T_2^* was determined by the mean absolute difference between the estimated and actual T_2 and T_2^* values.

2.3 | MR study

All images were acquired at 3.0 T (Siemens Magnetom SkyraFit, Erlangen, Germany) using a 32-channel head RF coil (Siemens, Erlangen, Germany) for signal reception and the body RF coil for transmission. Before each scan session, volume-selective B_0 shimming of the brain was applied. All imaging data were corrected for gradient delays⁶⁹ using additional calibration data, which were acquired before each 2in1-RARE-EPI scan. In accordance with the method proposed by Block et al,⁶⁹ calibration scans were performed for the phase encoding, and the read-out direction and an interpolation of the respective gradient delays was used for the correction of intermediate view angles. To make the correction more robust, the k-space shift was averaged over 4 calibration scans. In total, this resulted in 16 shots for the whole calibration scan (TA = 32 s).

Images were reconstructed using regridding with linear density compensation⁷⁰⁻⁷³ and a magnitude sum-of-squares channel combination. MSE and MGRE echo techniques (Siemens) were used as reference acquisition methods for T_2 and T_2^* mapping, respectively. The imaging parameters used for the phantom and in vivo studies are summarized in Table 1.

2.4 | T_2 and T_2^* mapping

For T_2 and T_2^* mapping images were reconstructed from k-space data acquired at the same TE (TE images). A linear least-square-fit of the logarithmic signal magnitude of the TE images was used to calculate the T_2 and T_2^* maps. The last TE image of the RARE module was included as the first TE image for T_2^* mapping. To determine the goodness-of-fit of the linear regression, R^2 maps (coefficient of determination) were calculated according to Equation (3), where y_i and f_i denote the logarithmic signal intensity and the corresponding fitted value at echo time, i , respectively.

$$R^2 = 1 - \frac{\sum_i (y_i - f_i)^2}{\sum_i (y_i - \bar{y})^2} \quad (3)$$

TABLE 1 Overview of the MR imaging parameters used for the phantom study and for the in vivo examinations

Pulse sequence	FOV [mm ²]	Matrix size	Radial		TR [ms]	No. of echoes	Echo spacing (ESP) [ms]	BW [Hz/px]	No. of shots	FA [°]	No. of slices	TA [min:s]
			views/PE lines	Resolution [mm ³]								
2in1-RARE-EPI	212 × 212 (232 × 232)	256 × 256	6200	0.83 × 0.83 × 5 (0.91 × 0.91 × 5)	2000	$N_{\text{RARE}} = 14$ $N_{\text{EPI}} = 18$	ESP _{RARE} = 6.5 ESP _{EPI} = 2.3	610	200	90, 180	1 (3)	07:12
Reference methods												
MSE	192 × 192 (232 × 232)	256 × 256	256	0.75 × 0.75 × 5 (0.91 × 0.91 × 5)	2000	15	8.9	610	256	90, 180	1 (3)	08:36
MGRE	212 × 212 (232 × 232)	256 × 256	256	0.83 × 0.83 × 5 (0.91 × 0.91 × 5)	40 (50)	12	2.27	610	256	12 (20)	1 (3)	0:14 (0:50)

Parameters used in the in vivo study, which differ from those used in the phantom study, are in parentheses. The number of shots in case of 2in1-RARE-EPI (200) corresponds to a 2-fold undersampling of the k-space for the TE images. Note that the acquisition time for MGRE in the in vivo study is increased compared to the phantom study because multiple slices were acquired sequentially in MGRE.

Abbreviations: BW, receiver bandwidth; FA, flip angle; TA, acquisition time.

Because of stimulated echoes, there is a signal change between the first and second echo, as can be seen in the signal decay depicted in Figure 1H. To account for this, we used a dummy echo in the 2in1-RARE-EPI. This might still lead to misestimations of T_2 , especially for short T_2 values. For the compensation of stimulated echoes, a fitting method based on extended phase graphs can be used, which incorporates the first echo of the T_2 decay.⁷⁴

2.5 | Phantom study

To examine the feasibility of simultaneous T_2 and T_2^* mapping with 2in1-RARE-EPI, a phantom study was performed. An in-house constructed phantom (Figure 1C-G) was used to mimic the T_2 and T_2^* of brain tissue. The phantom consisted of an array of 12 plastic tubes (volume = 15 mL, diameter = 15 mm) filled with water doped with varying concentrations of the iron oxide nanoparticle-based contrast agent Resovist (Schering, Berlin, Germany), which modifies T_2 and T_2^* of the solvent.⁷⁵⁻⁷⁸ The iron concentrations of the different solutions ranged between 2.3 to 12.3 $\mu\text{g Fe/mL}$ (Figure 1F). Based on the relaxivity $r_2^* = 5.2 \pm 0.1 \text{ mL } \mu\text{g}^{-1} \text{ s}^{-1}$ of the contrast agent reported in a previous study⁷⁸ and an $R_{2,\text{water}}^* = 1.35 \text{ s}^{-1}$, calculated from data provided in Dahnke and Schaeffter⁷⁸, this yields T_2^* values in the range of 15 ms to 83 ms. According to the relaxivity $r_2 = 2.56 \pm 0.2 \text{ mL } \mu\text{g}^{-1} \text{ s}^{-1}$ of the contrast agent⁷⁶ and an $R_{2,\text{water}} = 0.32 \pm 0.06 \text{ s}^{-1}$,⁷⁶ this results in T_2 values ranging between 31 ms and 161 ms.

2.6 | Ethics statement

For the in vivo feasibility study, approval by the local ethical committee (Charité-Universitätsmedizin, Berlin, Germany, EA1/191/19) was obtained before the study. Informed written consent was obtained from each volunteer before the study.

2.7 | In vivo study

To demonstrate the feasibility of simultaneous T_2 and T_2^* mapping with 2in1-RARE-EPI, in vivo examinations were performed on healthy volunteers ($n = 3$, sex: female [1]/male [2], age: 31-46 years, body mass index [BMI]: 23.6-25.9 kg/m^2) and MS patients ($n = 4$, sex: female [3]/male [1], age: 30-39 years, BMI: 22.3-34.9 kg/m^2). For the healthy volunteers, 3 brain slices covering the lateral ventricles were acquired. This brain area was chosen because it contains prominent anatomic features and because MS lesions frequently occur in the periventricular white matter.

In the patient cohort, MS-specific lesions were selected to be imaged with the 2in1-RARE-EPI, based on a transversal 2D T_2 -weighted RARE scan. The lesions were identified from 2D T_2 -weighted RARE images. The anatomic positions of the MS lesions are illustrated on sagittal and transversal views of images from a T_2 -weighted 3D SPACE pulse sequence (Siemens) acquisition (TR = 2050 ms, TE = 712 ms, 1 mm isotropic resolution). For multi-slice MR acquisitions, an interleaved acquisition scheme was used for 2in1-RARE-EPI and MSE, and a sequential slice acquisition was used for MGRE.

2.8 | Scatter and Bland-Altman plot analysis

Agreement between T_2 and T_2^* maps obtained with the 2in1-RARE-EPI method and the reference methods was evaluated using scatter plot and Bland-Altman (BA) plot analysis on values from selected regions of interest (ROIs). For the phantom study, 6 ROIs (size: 9×9 pixels) with varying iron concentration were placed within different tubes and 1 ROI within the main body of the phantom as outlined in Figure 1E by blue and red squares, respectively. For the analysis of the data obtained from healthy subjects, 6 ROIs (size: 7×7 pixels) were placed bilaterally in 3 brain regions: the globus pallidus, thalamus, and frontal (perivascular) white matter of the brain (Figure 1F,G). For the patient cohort, 8 ROIs (size: 7×7 pixels) covering selected MS lesions in 4 patients were used for the analyses. Before the scatter and BA plot analysis, T_2 and T_2^* maps obtained with 2in1-RARE-EPI and the reference methods were co-registered to correct for translational displacement because of bulk head motion. For this purpose, difference maps between the T_2 and T_2^* reference maps and the T_2 and T_2^* maps obtained with 2in1-RARE-EPI were calculated for 8 translational shifts of the reference maps by 1 pixel relative to the maps obtained with 2in1-RARE-EPI including diagonal shifts. The shift that provided clearly reduced values in the difference maps at sharp anatomic boundaries, determined by visual inspection, was applied to the reference maps before the scatter and BA analysis. Multiple linear regression was used to assess the agreement between the methods while also accounting for the effects of ROI and subject, and their interaction. In some cases, the differences of T_2 and T_2^* values among the respective methods did not follow a Gaussian distribution, and therefore the median of the T_2 and T_2^* differences, $M(\Delta T_2)$ and $M(\Delta T_2^*)$ and the interquartile range (iQR) were used to calculate the limits-of-agreement ($LOAs$) shown on the BA plots according to Equation (4)

$$LOAs = M\left(\Delta T_2^{(*)}\right) \pm 1.45 \cdot iQR. \quad (4)$$

3 | RESULTS

3.1 | Monte Carlo simulations

Monte Carlo simulations were performed to determine the number of echoes, N_{RARE} and N_{EPI} , for which the errors in the T_2 and T_2^* estimation are minimized. The map in Figure 2A shows the maximum error in T_2 AND T_2^* estimations for all T_2 and T_2^* combinations and SNRs used in the simulations as a function of the number of RARE and EPI echoes. The plot shows that the maximum absolute error is substantially decreased for $N_{\text{RARE}} = 13-15$ and for $N_{\text{EPI}} = 18-20$. Based on this finding, an echo train length of 32 echoes was used for 2in1-RARE-EPI imaging of phantoms and human subjects comprising 14 RARE echoes followed by 18 EPI echoes. For this configuration of RARE and EPI echoes the plot of the absolute error in T_2 and T_2^* over SNR is depicted in Figure 2B. These data show that the estimated absolute error in T_2 and T_2^* is lower than 2 ms for SNRs larger than 20. In comparison to the maximum absolute error, the maximum relative error in T_2 and T_2^* is minimized for a slightly lower number of RARE and EPI echoes (Figure 2C,D). For the imaging study, $N_{\text{RARE}} = 14$ and $N_{\text{EPI}} = 18$ was used because we considered the minimization of the absolute error to be of higher priority in cases where small variations of the relaxation time constants are relevant. The SNR estimates for the 2in1-RARE-EPI in the phantom study yielded an SNR within the 13 ROIs ranging from 160 to 260. The SNR estimates for the 2in1-RARE-EPI in a healthy subject yielded an SNR between 90 and 120 for the ROIs within the thalamus and globus pallidus and between 180 and 210 for ROIs within the frontal white matter. This is well beyond the SNR range used in the simulations. This shows that the SNR drop in the EPI module because of the T_2 decay is not consequential. In cases of very short T_2 values, the length of the RARE and EPI module can be adapted. Further simulations including a T_2 value of 50 ms yielded relative errors of $\sim 5\%$ for a T_2^* of 20 ms. In this case, the ideal number of echoes changes to $N_{\text{RARE}} = 8$ and $N_{\text{EPI}} = 13$.

3.2 | Phantom study

T_2 , T_2^* , and R^2 maps obtained from the phantom study are depicted in Figure 3 together with selected TE images. The depicted TE images highlight that the image quality is not impaired by the radial undersampling. The parametric maps demonstrate the decrease in T_2 and T_2^* with increasing iron concentration. The tubes containing identical iron concentration (Figure 1G) revealed similar T_2 and T_2^* values. The T_2 map obtained with 2in1-RARE-EPI is in agreement with the

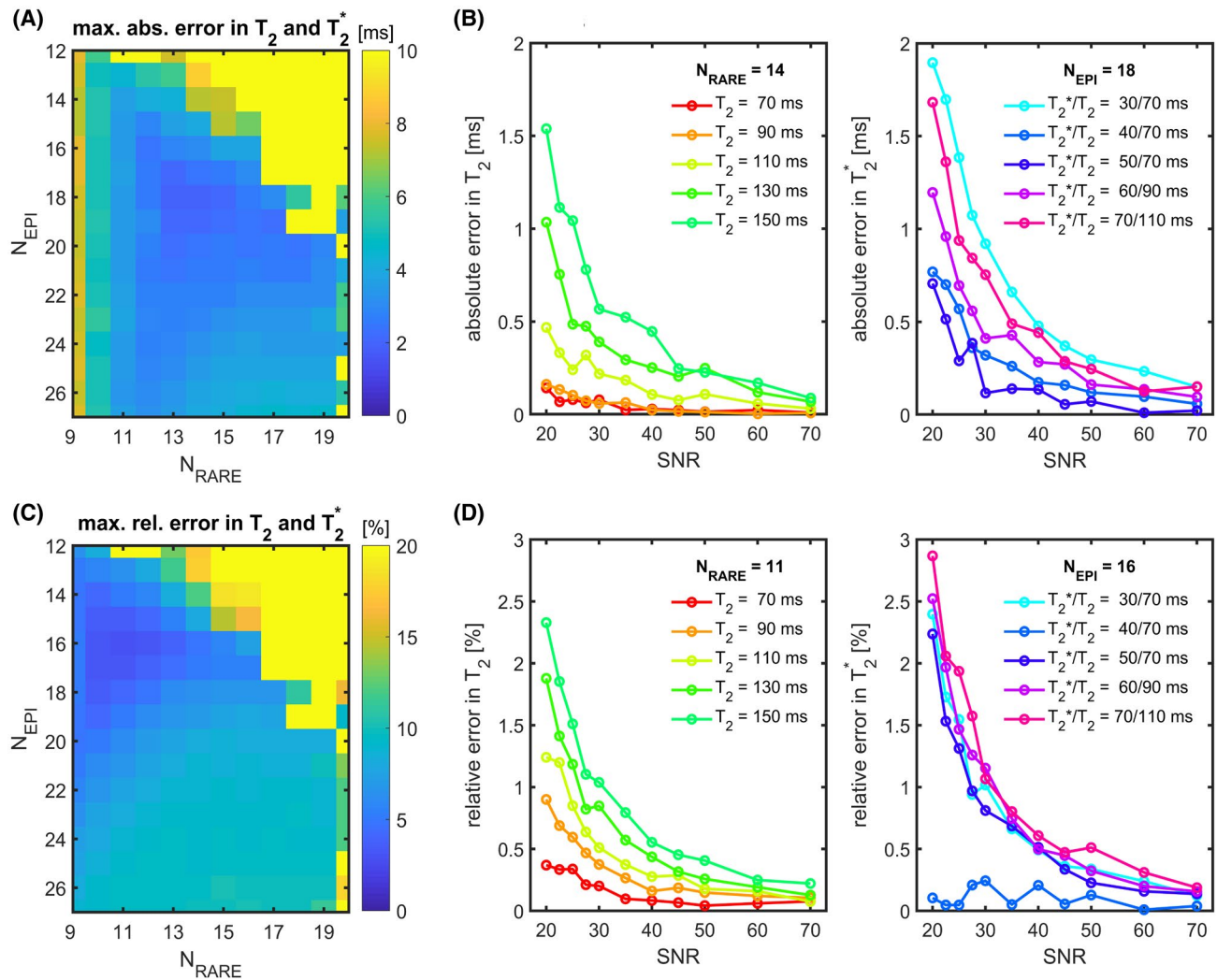


FIGURE 2 Results of Monte Carlo simulations of T_2 and T_2^* estimation errors. (A) Maximum absolute error in T_2 and T_2^* for a varying number of echoes used in the RARE and EPI module (N_{RARE} and N_{EPI}) and SNRs ranging between 20 and 70. The maximum absolute error in T_2 and T_2^* is minimized for $N_{RARE} = 14$ and $N_{EPI} = 18$. (B) The absolute error in T_2 (left) and T_2^* (right), for $N_{RARE} = 14$ and $N_{EPI} = 18$ and different combinations of T_2 and T_2^* values, as a function of SNR. (C) Maximum relative error in T_2 and T_2^* for varying N_{RARE} and N_{EPI} and SNRs ranging between 20 and 70. The maximum relative error in T_2 and T_2^* is minimized for $N_{RARE} = 11$ and $N_{EPI} = 18$. (D) The relative error in T_2 (left) and T_2^* (right), for $N_{RARE} = 11$ and $N_{EPI} = 16$ and different combinations of T_2 and T_2^* , as a function of SNR

reference T_2 map deduced from MSE (Figure 3, top panel). The corresponding R^2 maps show values close to 1, indicating a low fraction of unexplained variance in the logarithmic signal intensity, based on the T_2 values obtained with linear regression. The T_2^* maps obtained with the proposed 2in1-RARE-EPI approach accord well with those deduced from the MGRE reference (Figure 3, bottom panel). The corresponding R^2 maps exhibit lower R^2 values compared to those obtained for the T_2 mapping.

Quantitative comparisons of the T_2 and T_2^* values derived from 2in1-RARE-EPI acquisitions versus those obtained with reference methods (MSE and MGRE), and 2in1-RARE-EPI with $N_{RARE} = 1$ versus MGRE are shown in Figure 4. For this comparison, 13 ROIs (size: 9×9 pixels) were placed in the phantom as shown in Figure 1G.

Figure 4A shows the mean of the $R_2 = 1/T_2$ and $R_2^* = 1/T_2^*$ values within the ROIs as a function of the iron concentrations. As a comparison R_2 and R_2^* values, calculated from relaxivities provided by previous studies,^{76,78} are depicted as black lines. For R_2 , the measured values deviate from the calculated values. The mean R_2 values obtained with 2in1-RARE-EPI match those obtained with MSE, especially for the lower iron concentrations. For both methods, the relaxivity agrees well with the values provided in the literature.⁷⁶ For R_2^* , the measured values are in agreement with the calculated reference R_2^* values.

The results of the scatter and BA plot analysis are shown in Figure 4B,C. For T_2 , the multiple regression analysis shows a strong relationship between 2in1-RARE-EPI and MSE (accounting for the different iron concentrations

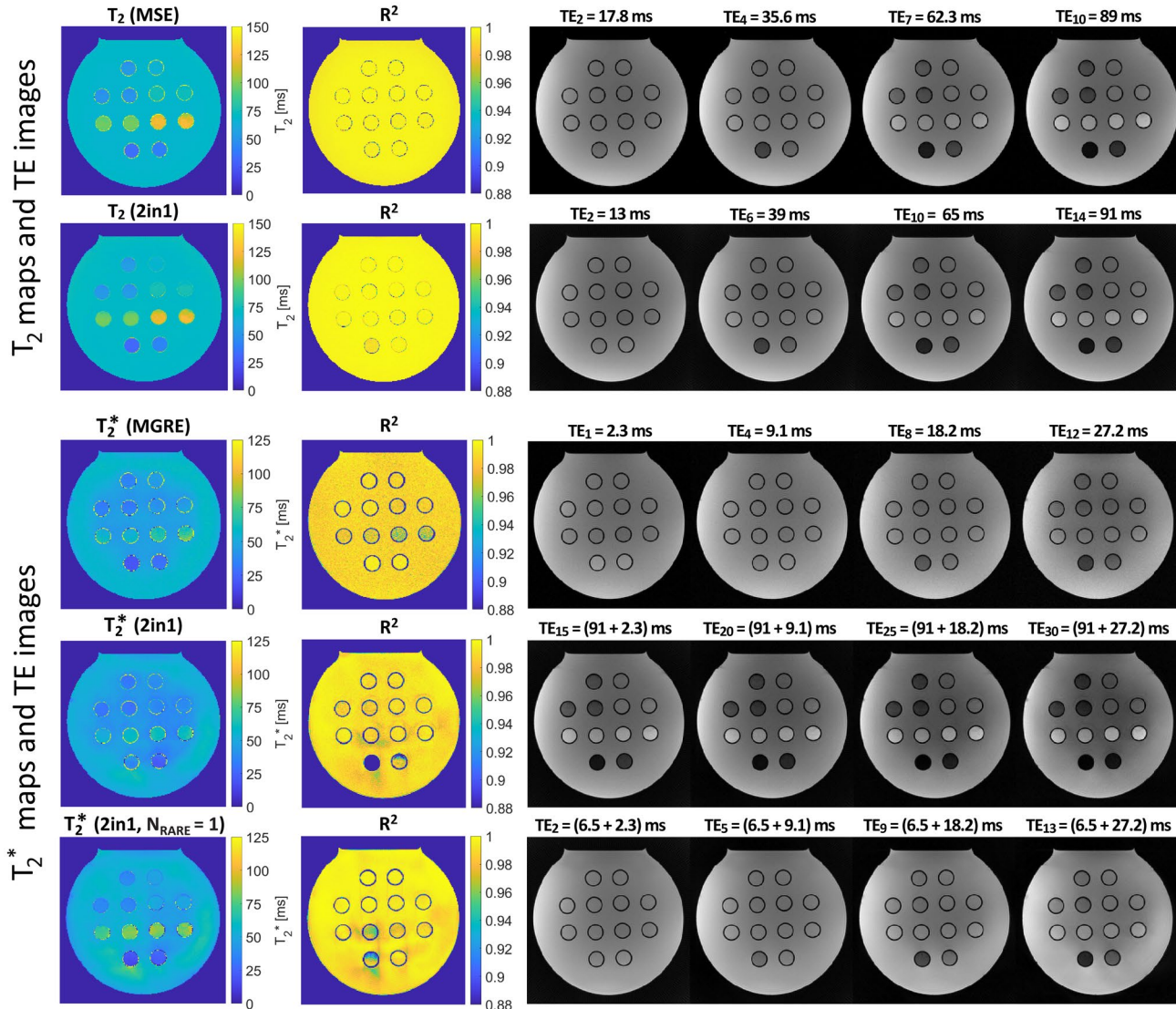


FIGURE 3 T_2 , T_2^* , and R^2 maps (coefficient of determination) and selected TE images of an in-house built phantom containing plastic tubes filled with varying concentrations of iron oxide nanoparticles. The iron concentrations of the solutions in the tubes and the body of the phantom are listed in Figure 1. The intensity of each TE image is normalized with respect to the minimum and maximum intensity. A good agreement was observed between the T_2 map obtained with 2in1-RARE-EPI and the reference T_2 map obtained with MSE, and between the T_2^* map derived from 2in1-RARE-EPI and the reference T_2^* map deduced from MGRE. The selected TE images highlight that the image quality is not impaired by the radial undersampling

within the ROIs): $F[13,553] = 9427$, adjusted $R^2 = 0.995$, $P < 2.2 \times 10^{-16}$. The BA plot analysis yielded a median difference of $M(\Delta T_2) = 1.6$ ms between the T_2 values, and LOAs of 4.6 and -1.4 ms. The scatter plot used for benchmarking T_2^* obtained from 2in1-RARE-EPI against MGRE also shows a good agreement between the methods, $F[13,553] = 2497$, adjusted $R^2 = 0.983$, $P < 2.2 \times 10^{-16}$, which is confirmed by the BA plot with $M(\Delta T_2^*) = -4.8$ ms and LOAs of 1.5 ms and -11.0 ms. The comparison between the 2in1-RARE-EPI with $N_{\text{RARE}} = 1$ and MGRE yielded similar results, $F[13,553] = 2815$, adjusted $R^2 = 0.985$, $P < 2.2 \times 10^{-16}$, although the BA plot showed a broader range of differences, with $M(\Delta T_2^*) = 3.7$ ms, and LOAs of 15.8 ms and -8.5 . Overall, these results demonstrate the good

correspondence between the T_2 and T_2^* relaxation times obtained simultaneously with 2in1-RARE-EPI and those derived from sequential MSE and MGRE acquisitions

3.3 | In vivo study

Next, the applicability of 2in1-RARE-EPI was demonstrated in an in vivo feasibility study involving healthy subjects. Figure 5 shows T_2 and T_2^* maps with the corresponding R^2 maps, and a selection of individual TE images of the brain of an exemplary healthy subject. The depicted TE images highlight that the image quality is not impaired by the radial undersampling. The T_2 maps obtained with 2in1-RARE-EPI

agreed with the maps from MSE. The corresponding R^2 maps obtained for 2in1-RARE-EPI and MSE exhibit high values, indicating a low fraction of unexplained variance in the logarithmic signal intensity for both methods. The T_2^* map obtained with 2in1-RARE-EPI accords with the T_2^* map deduced from MGRE. For both approaches, the R^2 values are lower than the corresponding R^2 values found for T_2 estimations. Note that the TE images acquired with the EPI module of 2in1-RARE-EPI feature a mixed T_2 and T_2^* weighting. The TE images obtained with the 2in1-RARE-EPI with $N_{RARE} =$

1 show a similar T_2^* weighting as the TE images obtained with the MGRE. Consistent with the phantom study, the R^2 values of the T_2^* map of the 2in1-RARE-EPI ($N_{RARE} = 1$) are slightly higher compared to the corresponding values for the 2in1-RARE-EPI ($N_{RARE} = 14$).

Quantitative comparisons of T_2 and T_2^* values between 2in1-RARE-EPI and the reference methods are shown in Figure 6 including data from all 3 healthy subjects. T_2 and T_2^* values were calculated in 6 ROIs (size: 7×7 pixels), which were placed within regions where MS lesions typically

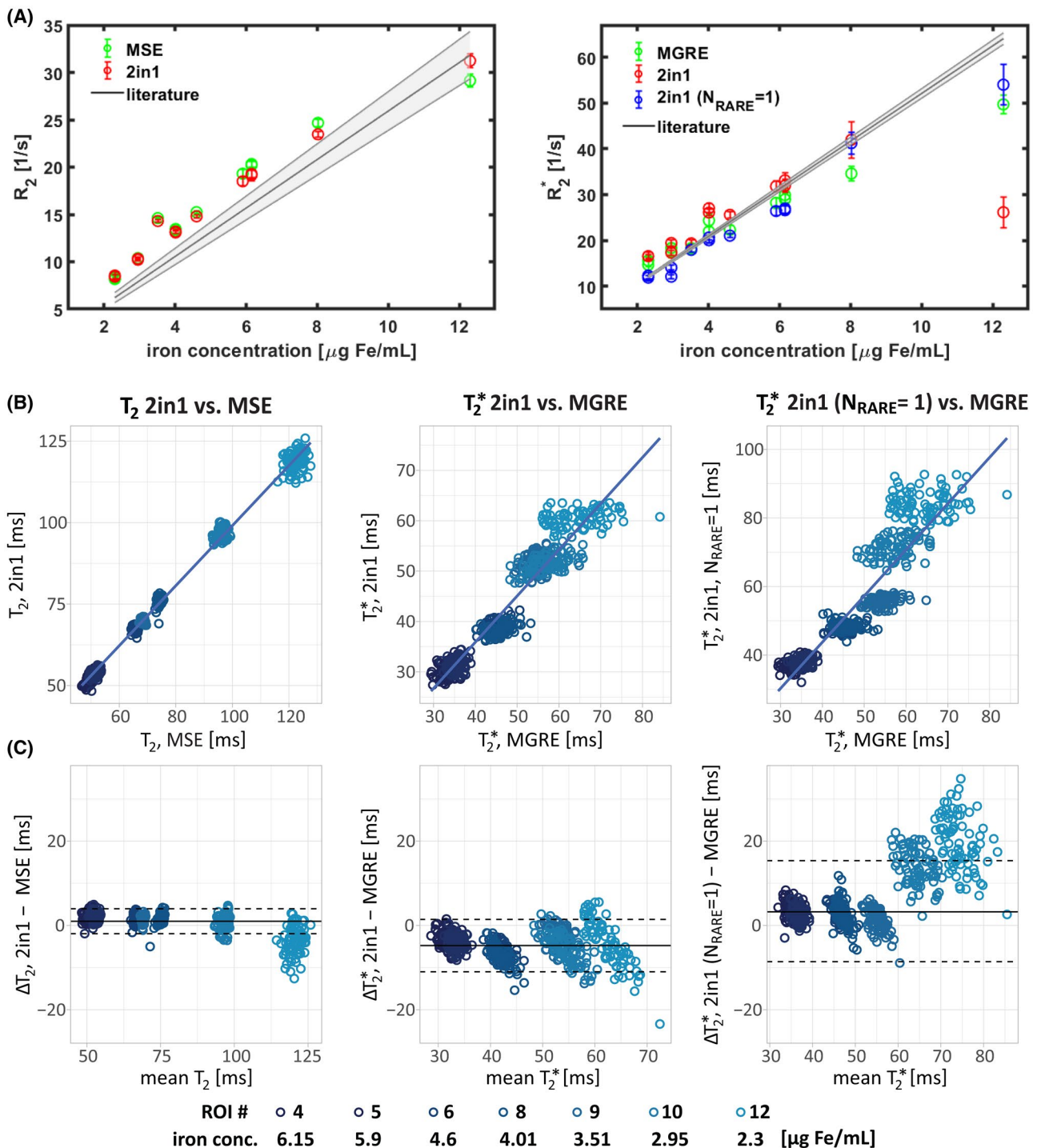


FIGURE 4 Quantitative comparisons of the T_2 and T_2^* values obtained from the phantom studies presented in Figure 3. (A) Mean relaxation rates $R_2 = 1/T_2$ and $R_2^* = 1/T_2^*$ (taken from 13 ROIs, size: 9×9 pixel, placed within the phantom, see Figure 1), as a function of the iron concentration of the solutions corresponding to the ROIs. Error bars indicate the SD of the values within the ROIs. For comparison the calculated R_2 and R_2^* values, based on the relaxivities of the contrast agent and the intercepts reported by previous studies ($r_2 = 2.6 \pm 0.2 \text{ mL } \mu\text{g}^{-1} \text{ s}^{-1}$, $R_{2,\text{water}} = 0.32 \pm 0.06 \text{ s}^{-1}$, and $r_2^* = 5.2 \pm 0.1 \text{ mL}/\mu\text{g}^{-1} \text{ s}^{-1}$, $R_{2,\text{water}}^* = 0.09 \text{ s}^{-1}$)^{76,78} are depicted as solid black lines. The margin of error is indicated by a grey shade. $R_{2,\text{water}}^*$ was calculated from data provided in Dahnke and Schaeffter.⁷⁸ $R_{2,\text{water}}$ and r_2 were measured at 37°C ,⁷⁶ whereas our phantom study was conducted at room temperature. (B) Scatter plots comparing T_2 and T_2^* values derived from 2in1-RARE-EPI acquisitions versus those obtained with reference methods (MSE and MGRE) and 2in1-RARE-EPI with $N_{\text{RARE}} = 1$ versus MGRE. Color of the data points is scaled with iron concentration, indicated at the bottom of the figure. Multiple linear regression shows a strong relationship between the values obtained with 2in1-RARE-EPI and the reference methods, while accounting for the effect of different iron concentration: 2in1-RARE-EPI versus MSE: $F[13,553] = 9427$, adjusted $R^2 = 0.995$, $P < 2.2 \times 10^{-16}$; 2in1-RARE-EPI versus MGRE: $F[13,553] = 2497$, adjusted $R^2 = 0.983$, $P < 2.2 \times 10^{-16}$; 2in1-RARE-EPI with $N_{\text{RARE}} = 1$ versus MGRE: $F[13,553] = 2815$, adjusted $R^2 = 0.985$, $P < 2.2 \times 10^{-16}$. (C) BA plots corresponding to the scatter plots shown in (B). The following values for the median of the T_2 and T_2^* differences (solid black line) and the upper and lower limits-of-agreement ($LOAs = M(\Delta T_2^*) \pm 1.45 \times iQR$, dashed black line) were obtained from the BA plot analysis: 2in1-RARE-EPI versus MSE: $M(\Delta T_2) = 1.6 \text{ ms}$, $LOAs = 4.6 \text{ ms}$ and -1.4 ms ; 2in1-RARE-EPI versus MGRE: $M(\Delta T_2^*) = -4.8 \text{ ms}$, $LOAs = 1.5 \text{ ms}$ and -11.0 ms and 2in1-RARE-EPI with $N_{\text{RARE}} = 1$ versus MGRE: $M(\Delta T_2^*) = 3.7 \text{ ms}$, $LOAs = 15.8 \text{ ms}$ and -8.5 ms

emerge: globus pallidus, thalamus, and frontal (perivascular) white matter (Figure 1H). Multiple regression analysis of the T_2 values shows a strong relationship between the proposed 2in1-RARE-EPI and the reference method MSE, accounting for effects of the different anatomic regions and different subjects, and their interactions: $F[17,864] = 118.6$, adjusted $R^2 = 0.6942$, $P = 3.75 \times 10^{-212}$. The regression analysis for the T_2^* comparison between 2in1-RARE-EPI and MGRE revealed a strong relationship: $F[17,864] = 46.48$, adjusted $R^2 = 0.4674$, $P = 2.50 \times 10^{-309}$. The T_2^* comparison between 2in1-RARE-EPI ($N_{\text{RARE}} = 1$) and MGRE yielded similar results: $F[17,864] = 40.59$, adjusted $R^2 = 0.4331$, $P = 7.46 \times 10^{-98}$ (Figure 6A). These results were supported by the BA plots: 2in1-RARE-EPI versus MSE: $M(\Delta T_2) = 0.3 \text{ ms}$ with $LOAs$ of 6.5 ms and -5.8 ms ; 2in1-RARE-EPI versus MGRE: $M(\Delta T_2^*) = 3.1$ with $LOAs$ of 18.5 ms and -12.3 ms ; 2in1-RARE-EPI ($N_{\text{RARE}} = 1$) and MGRE: $M(\Delta T_2^*) = -2.1 \text{ ms}$, $LOAs$ of 10.4 ms and -14.6 ms (Figure 6B).

Following the feasibility study in healthy subjects, 2in1-RARE-EPI was applied in MS patients. Figure 7 depicts T_2 and T_2^* maps of the brain of a 30-year-old female MS patient. The parametric maps show 3 periventricular MS lesions adjacent to the right lateral ventricle. The first 2 columns of Figure 7 highlight an MS lesion adjacent to the posterior horn of the right lateral ventricle. The lesion clearly appears hyperintense in the T_2 map. The T_2 map obtained with 2in1-RARE-EPI is in good accordance with the T_2 map derived from MSE. The white matter lesion is also clearly delineated in the T_2^* maps calculated from 2in1-RARE-EPI and MGRE data. The third and fourth columns of Figure 7 highlight 2 lesions adjacent to the anterior and posterior horns of the right lateral ventricle. Both lesions are clearly delineated in the T_2 and T_2^* maps obtained with 2in1-RARE-EPI and with the reference methods MSE and MGRE.

T_2 and T_2^* maps obtained from a 54-year-old male MS patient are shown in Figure 8. Sagittal and transversal anatomic views in the first row of Figure 8 show 2 lesions, targeted for

T_2 and T_2^* mapping with 2in1-RARE-EPI and the reference methods (MSE and MGRE). The first 2 columns of Figure 8 show T_2 and T_2^* maps highlighting a periventricular lesion adjacent to the right lateral ventricle. The lesion is clearly delineated in the T_2 and T_2^* maps. The third and fourth columns show T_2 and T_2^* maps highlighting a juxtacortical lesion located in the left posterior hemisphere. This lesion is also clearly delineated in the T_2 and T_2^* maps. The maps derived from 2in1-RARE-EPI are consistent with those from MSE and MGRE imaging.

Quantitative comparisons of the T_2 and T_2^* values obtained from the MS patients using the 2in1-RARE-EPI versus the reference methods are shown in Figure 9. T_2 and T_2^* values were obtained from ROIs corresponding to the location of the lesions shown in the representative images in Figures 7 and 8 (size: 7×7 pixels). Data from 2 additional patients is included in the quantitative analysis, for a total of 8 ROIs corresponding to separate lesions. Multiple regression analysis of the T_2 values shows a strong relationship between the proposed 2in1-RARE-EPI and the reference method MSE, accounting for effects of the different patients, and their separate lesions (a separate regression line is shown for each lesion): $F[8,383] = 577.2$, adjusted $R^2 = 0.9218$, $P = 2.01 \times 10^{-208}$. The regression analysis for the T_2^* comparison between 2in1-RARE-EPI and MGRE revealed a strong relationship: $F[8,383] = 137$, adjusted $R^2 = 0.7356$, $P = 2.12 \times 10^{-107}$. These results were supported by the BA plots: 2in1-RARE-EPI versus MSE: $M(\Delta T_2) = -0.3 \text{ ms}$ and $LOAs$ of 10.3 ms and -10.9 ms ; 2in1-RARE-EPI versus MGRE: $M(\Delta T_2^*) = 8.6 \text{ ms}$ with $LOAs$ of 25.1 ms and -7.5 ms ; (Figure 9B).

4 | DISCUSSION

This work demonstrates the feasibility of radially sampled 2in1-RARE-EPI for simultaneous T_2 and T_2^* mapping. Our

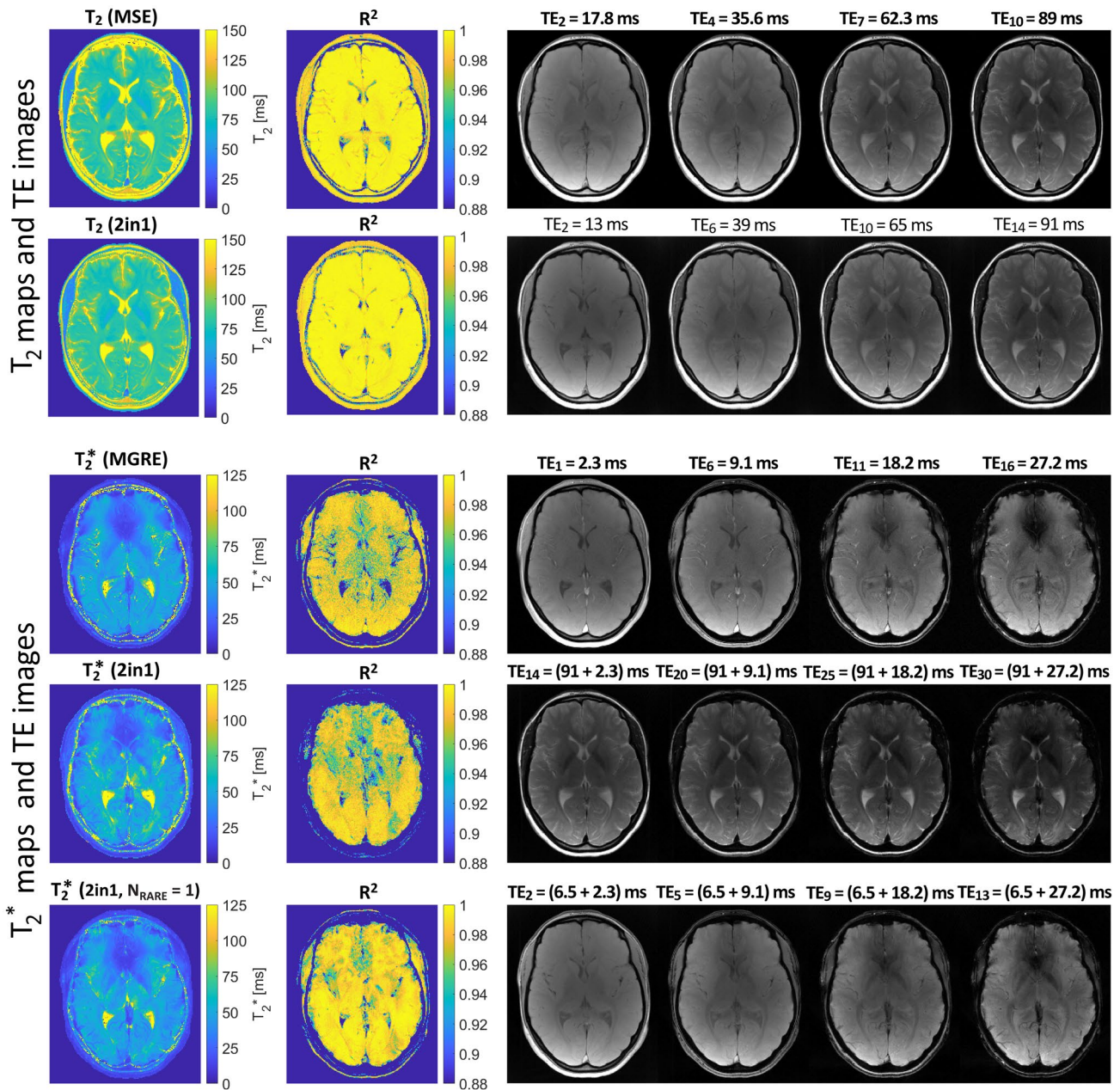


FIGURE 5 T_2 and T_2^* maps along with the R^2 maps (coefficient of determination) and selected TE images of the brain of a healthy female subject. The intensity of each TE image is normalized with respect to the minimum and maximum intensity within the brain tissue. The 2 rows at the top show the image data derived from the reference method MSE and those derived from 2in1-RARE-EPI. Good agreement between both T_2 maps was observed. Both R^2 maps exhibit R^2 values close to 1 throughout the brain. The 3 rows at the bottom show the image data derived from the reference method MGRE and those derived from 2in1-RARE-EPI and 2in1-RARE-EPI with $N_{\text{RARE}} = 1$. Good agreement was observed between the T_2^* maps derived by the different methods. The R^2 values observed in the 3 R^2 maps, although lower than those derived from the T_2 mapping with MSE and 2in1-RARE-EPI, are in a reasonable range. The selected TE images highlight that the image quality is not impaired by the radial undersampling

evaluation study in a phantom, equipped with solutions of different iron concentrations mimicking the T_2 and T_2^* relaxation properties of brain tissue, showed good agreement between the T_2 and T_2^* values obtained with 2in1-RARE-EPI and the reference parametric maps calculated from MSE and MGRE acquisitions. At low iron concentrations, there was a tendency for 2in1-RARE-EPI to slightly

underestimate the T_2 , compared to MSE, whereas T_2^* was rather overestimated compared to MGRE at low iron concentrations, but only for 2in1-RARE-EPI with $N_{\text{RARE}} = 1$. For the T_2^* values obtained with MGRE, a larger spread was observed compared to the T_2^* values obtained with 2in1-RARE-EPI, which leads to a slight trend in the BA plots, depending on the ROI. This observation is mainly

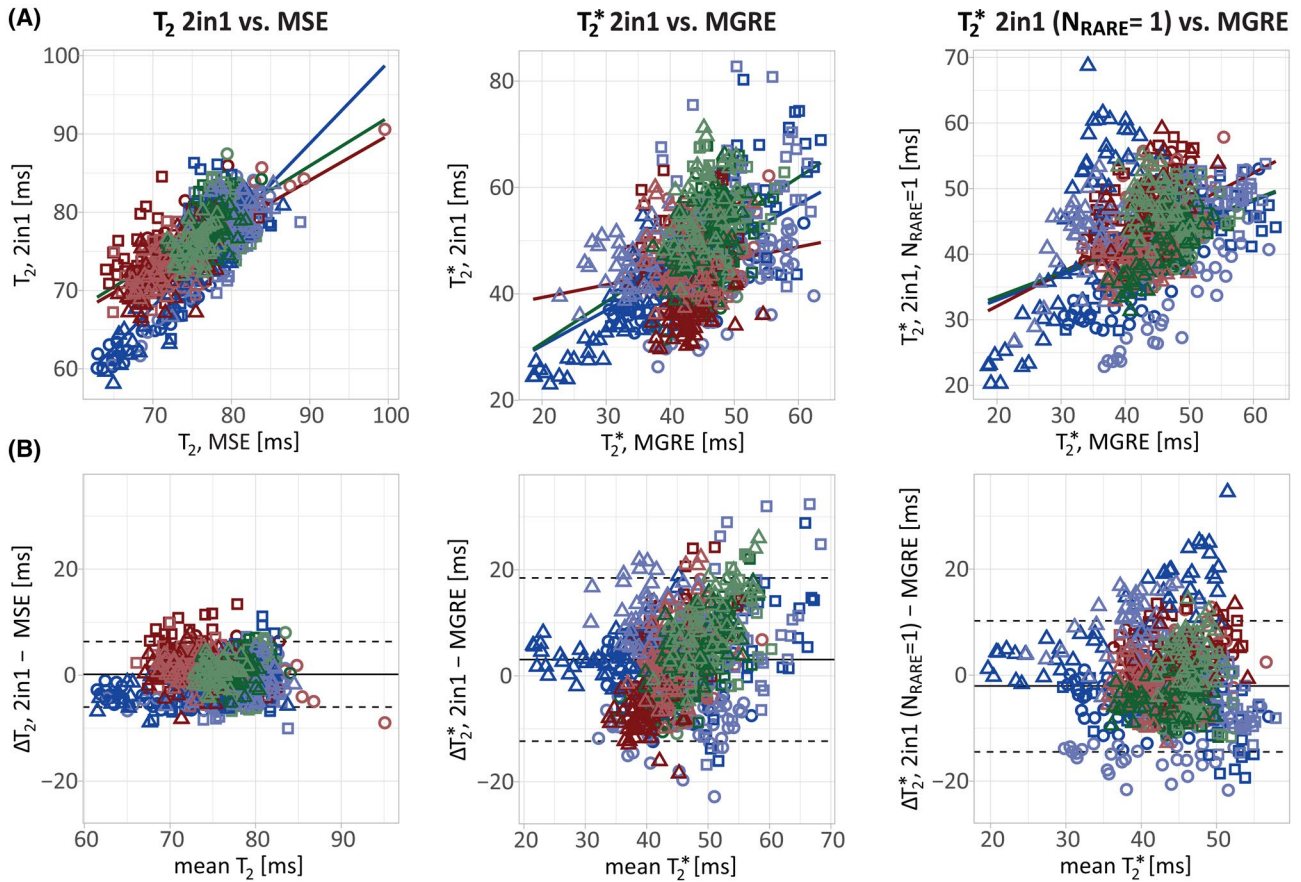


FIGURE 6 Results of the scatter and BA plot analysis of the T_2 and T_2^* values calculated from the brain scans of the 3 healthy subjects (denoted by square, circle, and triangle). Data points are colored according to the anatomical location of the ROIs (size: 7×7 pixels) as depicted in Figure 1F,G: thalamus, blue; globus pallidus, red; frontal white matter, green; left and right hemisphere = dark, light. (A) Scatter plots comparing T_2 and T_2^* derived from 2in1-RARE-EPI acquisitions versus those obtained with reference methods (MSE and MGRE), and 2in1-RARE-EPI with $N_{\text{RARE}} = 1$ versus MGRE. Multiple linear regression shows a strong relationship between the values obtained with 2in1-RARE-EPI and the reference methods, while accounting for the effect of different anatomical region and subject, and their interactions (separate regression lines for each anatomical region are depicted): 2in1-RARE-EPI versus MSE: $F[17,864] = 118.6$, adjusted $R^2 = 0.6942$, $P = 3.75 \times 10^{-212}$; 2in1-RARE-EPI versus MGRE: $F[17,864] = 46.48$, adjusted $R^2 = 0.4674$, $P = 2.50 \times 10^{-309}$; 2in1-RARE-EPI with $N_{\text{RARE}} = 1$ versus MGRE: $F[17,864] = 40.59$, adjusted $R^2 = 0.4331$, $P = 7.46 \times 10^{-98}$. (B) BA plots corresponding to the scatter plots shown in (A). The following values for the median of the T_2 and T_2^* differences (solid black line) and limits-of-agreement ($LOAs = M(\Delta T_2^*) \pm 1.45 \times iQR$, dashed black line) were obtained from the BA plot analysis: 2in1-RARE-EPI versus MSE: $M(\Delta T_2) = 0.3$ ms, $LOAs = 6.5$ ms and -5.8 ms; 2in1-RARE-EPI versus MGRE: $M(\Delta T_2^*) = 3.1$ ms, $LOAs = 18.5$ ms and -12.3 ms; 2in1-RARE-EPI with $N_{\text{RARE}} = 1$ versus MGRE: $M(\Delta T_2^*) = -2.1$ ms, $LOAs = 10.4$ ms and -14.6 ms

because of a lower SNR in the MGRE images, which varies with the iron concentration because of the change in T_1 . The observed deviation of the measured R_2 values from the values calculated based on literature⁷⁶ can be related to the fact that the relaxivity of the contrast agent and $R_{2,\text{water}}$ were measured at 37°C ,⁷⁶ whereas our phantom study was conducted at room temperature. For the solution with the highest iron concentration an overestimation of T_2^* obtained with 2in1-RARE-EPI was observed. This could be because of the rather long EPI module compared to the short T_2^* values, leading to an increased noise level in later TE images, which is already increased because of the preceding T_2 decay. This finding has no adverse effect on the application of the 2in1-RARE-EPI for characterizing

pathophysiological changes in brain tissue during MS, because such low T_2 and T_2^* values are mainly not featured by the relevant tissues in the brain at 3.0 T.

The agreement of T_2 and T_2^* values obtained with the 2in1-RARE-EPI with the values obtained from reference methods was corroborated in the feasibility study conducted in healthy subjects. The patient study also demonstrated that MS lesions can be just as clearly distinguished in the T_2 and T_2^* maps obtained from 2in1-RARE-EPI acquisitions, when compared to reference maps derived from conventional T_2 and T_2^* mapping using MSE/MGRE techniques.

In the current feasibility study, the evaluation of simultaneous T_2 and T_2^* mapping with 2in1-RARE-EPI was restricted to MS lesions and tissues with intermediate to long

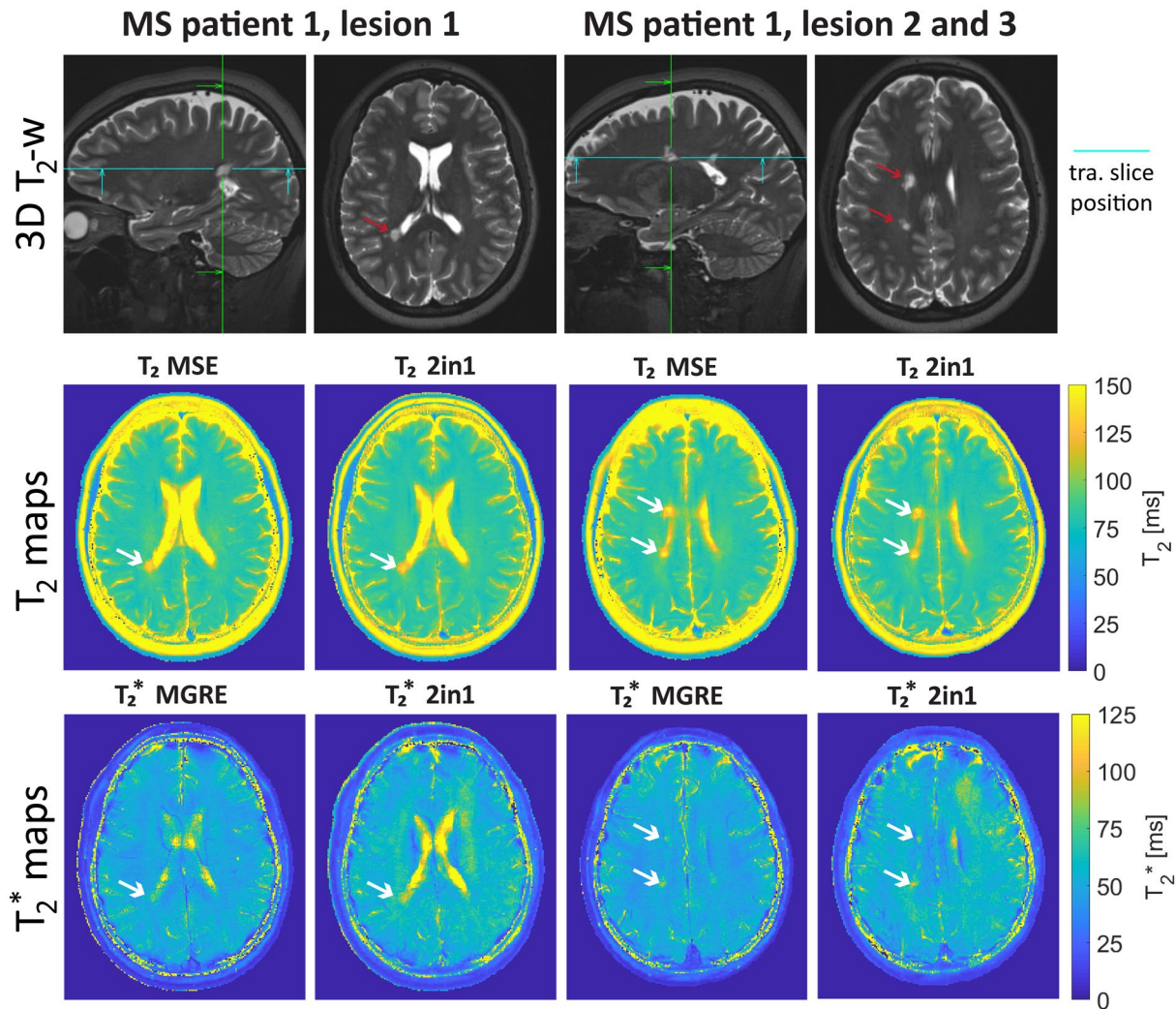


FIGURE 7 T₂ and T₂* maps of the brain of an MS patient (female, age: 30 years) obtained with 2in1-RARE-EPI and with reference methods MSE and MGRE. The position of the lesions targeted for T₂ and T₂* mapping are presented in sagittal and transversal views acquired with a T₂-weighted 3D SPACE pulse sequence (top row). The cyan line in the sagittal view indicates the position of the transverse slice. The first 2 columns depict a periventricular MS lesion located adjacent to the posterior horn of the right lateral ventricle (highlighted by white arrow). The third and fourth columns present T₂ and T₂* maps of 2 periventricular MS lesions adjacent to the right lateral ventricle. All 3 MS lesions are clearly delineated in the T₂ and T₂* maps. The maps acquired with 2in1-RARE-EPI are consistent with those obtained with MSE and MGRE

T₂ values. Further studies are needed to evaluate the performance of the method for tissues exhibiting low T₂ values (e.g., as a result of increased iron deposition), which is a pathological feature of some neurodegenerative diseases, including MS. In such cases, the length of the RARE and EPI modules can be adapted accordingly to achieve optimal results. Our proof-of-principle study used mono-exponential fitting for T₂ mapping. This approach yields a weighted average of tissue T₂, which might not be sufficiently specific for all brain pathologies. More pathology-specific information could be obtained using multi-exponential fitting to differentiate multiple relaxation components or tissue compartments. This approach would benefit the quantification of microstructural tissue changes, demyelination processes, and myelin water content,^{79,80} which may predict MS conversion.⁸¹

A caveat of our feasibility study is that it used a limited number of slices ($n = 3$) rather than whole brain coverage. To better adapt this approach to clinical requirements, the slice thickness (5 mm) could be reduced, which would decrease partial volume effects and yield a better coverage of lesions. Reducing the slice thickness would be feasible regarding the high SNR estimated for the 2in1-RARE-EPI with the parameters of the current study. The acquisition of more slices can be easily achieved without increasing the acquisition time because of the long TR used in 2in1-RARE-EPI.

The simultaneous acquisition of T₂ and T₂* maps with 2in1-RARE-EPI entails a trade-off between a long RARE module to decrease estimation errors for long T₂ values and a rather short RARE module to preserve SNR for the acquisition with the subsequent EPI module. Moreover, a short overall echo

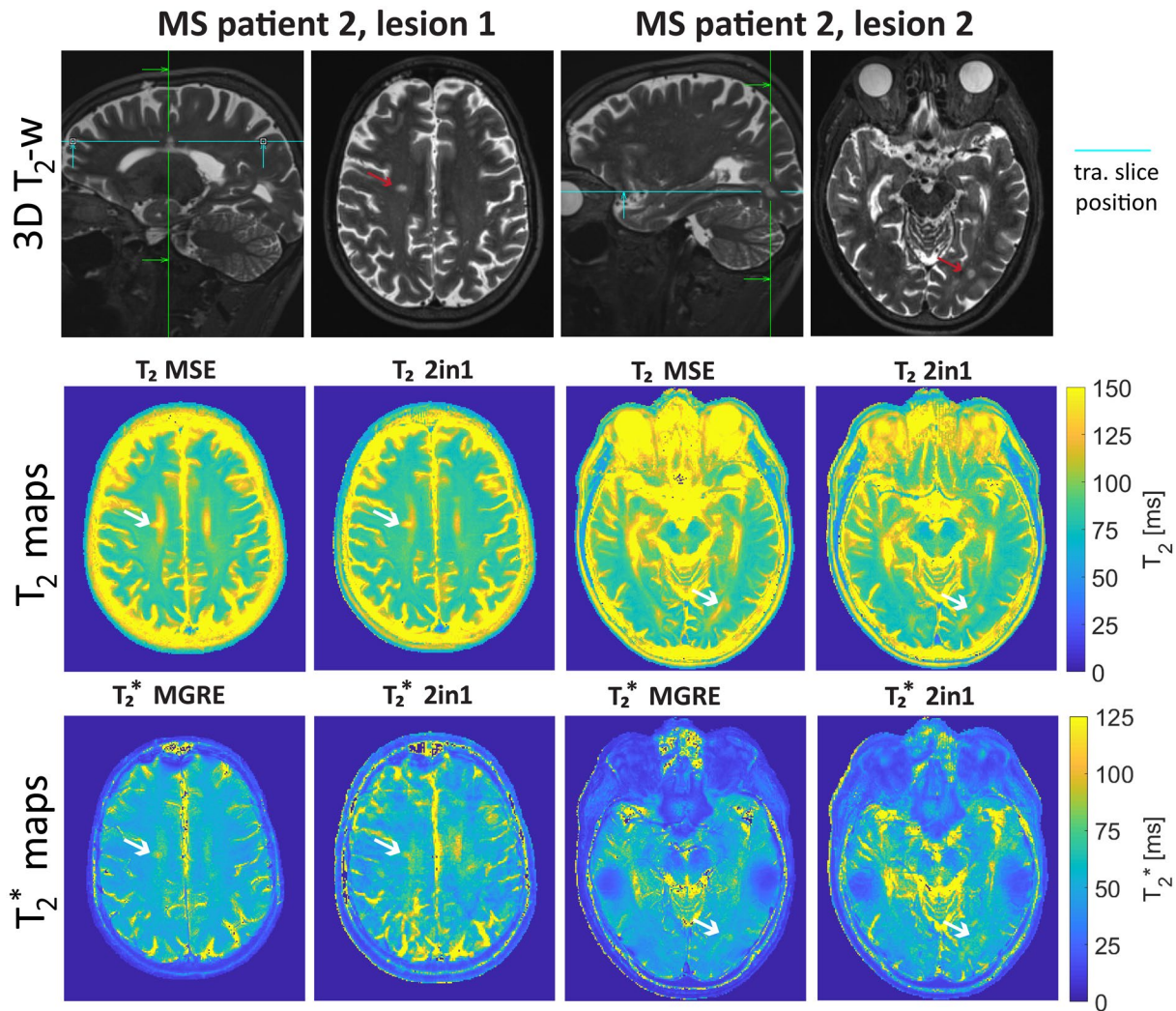


FIGURE 8 T_2 and T_2^* maps of the brain of an MS patient (male, age: 54 years) obtained with 2in1-RARE-EPI and with the reference methods MSE and MGRE. The position of the lesions targeted for T_2 and T_2^* mapping are presented in sagittal and transversal views acquired with a T_2 -weighted 3D SPACE (top row). The cyan line in the sagittal view indicates the position of the transverse slice. The first 2 columns show a periventricular MS lesion (highlighted by white arrow) located adjacent to the right lateral ventricle. The third and fourth columns show T_2 and T_2^* maps depicting a juxtacortical MS lesion in the left anterior hemisphere. Both lesions are clearly delineated in the T_2 and T_2^* maps. The maps acquired with 2in1-RARE-EPI are consistent with those obtained with MSE and MGRE

train length is desirable for optimal slice coverage efficiency in multi-slice acquisitions. Taking these considerations into account, our Monte Carlo simulations identified the appropriate numbers of RARE and EPI echoes for the respective modules needed to minimize the relative and absolute error in T_2 and T_2^* . These results were then incorporated into the phantom and the in vivo studies of healthy volunteers and MS patients.

MRI examinations targeting MS typically involve a series of multiple imaging contrasts and MR-metrics, resulting in long examination times and a greater propensity to motion artifacts and slice mis-registration.¹⁸⁻²⁰ Dual or multi-contrast techniques offer the potential for substantial scan time reduction. The undersampled 2in1-RARE-EPI hybrid approach used in the current study permits reduced acquisition time

for T_2 and T_2^* mapping compared to conventional sequential mapping methods. The EPI module in 2in1-RARE-EPI only slightly increases the echo train length within the long TR needed to account for T_1 effects. Unlike 2in1-RARE-EPI, MGRE uses a short TR promoted by a low flip angle. The short TR dictates that multiple slices are commonly acquired sequentially, which leads to a linear increase in the acquisition time with the number of slices. Consequently, increasing the number of slices to achieve whole-brain coverage emphasizes the scan time savings of 2in1-RARE-EPI compared to sequential T_2 and T_2^* mapping using MSE and MGRE. Further acceleration is promoted by radial undersampling of k-space. In this way, the acquisition time for T_2 and T_2^* maps of 3 slices was reduced to 76% using 2-fold undersampled 2in1-RARE-EPI. Assuming an imaging volume with 25

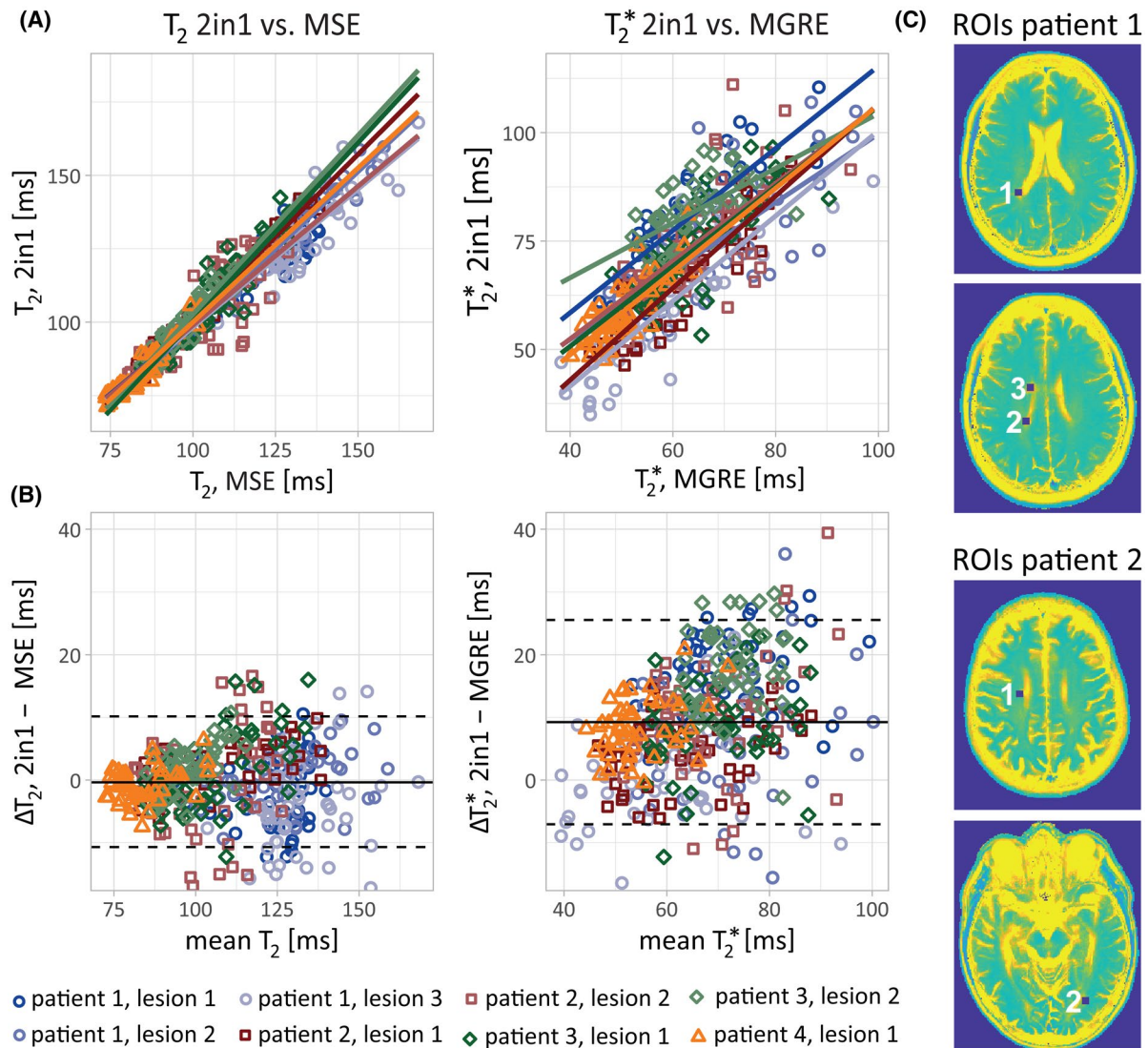


FIGURE 9 Results of the scatter plots (A) and BA plot (B) analysis of T_2 and T_2^* values obtained for the lesions from MS patients depicted in Figure 7 (circles) and 8 (squares), and lesions from 2 additional MS patients (triangles, diamonds). The analysis benchmarks 2in1-RARE-EPI against the sequential acquisition using the MSE and MGRE reference methods. Data points are colored according to the ROIs (size: 7×7 pixels) covering each separate lesion (8 lesions total). (A) Scatter plots comparing T_2 and T_2^* derived from 2in1-RARE-EPI acquisitions versus those obtained with reference methods (MSE and MGRE). Multiple linear regression shows a strong relationship between the values obtained with 2in1-RARE-EPI and the reference methods, while accounting for the effect of different patient and different lesions (separate regression lines for each individual lesion are depicted): 2in1-RARE-EPI versus MSE: $F[8,383] = 577.2$, adjusted $R^2 = 0.9218$, $P = 2.01 \times 10^{-208}$; 2in1-RARE-EPI versus MGRE: $F[8, 383] = 137$, adjusted $R^2 = 0.7356$, $P = 2.12 \times 10^{-107}$ (B) BA plots corresponding to the scatter plots shown in (A). The following values for the median of the T_2 and T_2^* differences (solid black line) and limits-of-agreement ($LOAs = M(\Delta T_2^{(*)}) \pm 1.45 \times iQR$, dashed black line) were obtained from the BA plot analysis: 2in1-RARE-EPI versus MSE: $M(\Delta T_2) = -0.3$ ms, $LOAs = 10.3$ ms and -10.9 ms; 2in1-RARE-EPI versus MGRE: $M(\Delta T_2^*) = 8.6$ ms, $LOAs = 25.1$ ms and -7.5 ms; (C) ROIs covering the lesions of patients 1 and 2

slices, the acquisition time could be reduced to 62% compared to the sequential acquisition with MSE/MGRE using Cartesian sampling.

Further acquisition time shortening can be enabled by multiband RF pulses for simultaneous multi-slice imaging. An unfortunate corollary of the RARE module is the number of refocusing pulses required, which might deteriorate the specific absorption rate economy of 2in1-RARE for simultaneous multi-slice imaging. Slice accelerated acquisition

schemes using power-independent number of slices RF pulses is a promising approach to offset RF power deposition while improving imaging speed and spatial coverage.⁸²⁻⁸⁴ The 2in1-RARE-EPI approach is compatible with the concept of hyperechoes⁸⁵ and variable refocusing flip angles⁸⁶ that can serve to further offset specific absorption rate for multiband applications.

Our study demonstrates that 2in1-RARE-EPI permits simultaneous T_2 and T_2^* mapping within clinically acceptable

scan times. Streamlining acquisition times is crucial for incorporating these important MR metrics into broader clinical studies, and ultimately into routine practice. Therefore, 2in1-RARE-EPI may provide a valuable contribution for enhancing and developing future MRI-based diagnostics and monitoring of MS and related disorders. Potential improvements may cover various aspects ranging from emerging MR techniques to track MS disease activity,^{5,8,9,23,87} including detection of transient enlargement of the ventricles during relapsing-remitting MS⁸⁸ and volumetric and microstructural measurements,⁸⁹⁻⁹² to the enhancement of our understanding of the underlying fundamental pathophysiology of the disease.¹² For example, the assessment of changes in T_2 could provide a more robust correlate for clinical disability than the T_2 lesion count.^{26,31} It has also been suggested that a prolongation of T_2 in NAWM could be an indicator for early MS.³⁰ Because of its sensitivity to iron deposition and its dependency on tissue myelination level, T_2^* mapping could provide insights into disease activity.⁴²⁻⁴⁴ Furthermore, T_2^* mapping might become a tool to assess MS already at an early stage of the disease.^{30,45} 2in1-RARE-EPI also promises to support the differential diagnosis of MS and other neurodegenerative diseases, including orphan diseases.^{14,15} This is beneficial in a clinical context, but also in preclinical studies involving experimental MS models in small rodents and nonhuman primates where multiple MR metrics are assessed.⁹³⁻⁹⁵ Moreover, simultaneous acquisition of multiple contrasts obviates the need for slice co-registration when combining multiple series of images. 2in1-RARE-EPI may also provide an endogenous contrast-based alternative for the assessment of the incidence of enhancing lesions or the lesion acuity in longitudinal MRI exams of MS patients, which commonly use exogenous intravenous gadolinium-based contrast agents for routine follow-up imaging.⁹⁶⁻⁹⁸

The T_2 and T_2^* maps derived from 2in1-RARE-EPI offer the capacity for the calculation of R_2' maps, which is conceptually appealing for probing the spatial distribution of magnetic susceptibility effects.^{99,100} This could be beneficial for the assessment of chronic active MS lesions that are characterized by a rim of iron-enriched activated microglia and macrophages, probing iron levels in the deep gray matter, and for identifying regions of demyelination and iron accumulation during the formation of MS lesions.¹⁰¹

The potential of the proposed 2in1-RARE-EPI hybrid is not limited to MS lesions or even brain imaging. 2in1-RARE-EPI offers the capacity for simultaneous T_2 and T_2^* mapping in applications dealing with bulk or physiological motion, such as cardiac imaging including myocardial T_2 and T_2^* mapping,¹⁰²⁻¹⁰⁴ as well as multi-parametric MRI of the eye, kidney, abdomen, and liver.¹⁰⁵⁻¹¹⁰ For these applications in moving organs, motion correction approaches such as 1D or 2D linear phase correction promise to ensure immunity

to bulk motion.^{111,112} The use of radial k-space trajectories shown in the current study holds the promise to render additional navigator data unnecessary because the densely sampled k-space center can be deployed for phase correction of motion corrupted data. This approach promotes self-calibrated motion compensation techniques.

5 | CONCLUSION

To conclude, the proposed 2in1-RARE-EPI hybrid constitutes a tool to advance quantitative mapping of T_2 and T_2^* particularly during brain pathology. The reduced scan time promotes patient comfort and is a fundamental precursor to boosting the implementation of quantitative mapping in clinical routine practice, and to conducting broader clinical studies on the potential of T_2 and T_2^* as biomarkers in MS. This work demonstrates the feasibility of 2in1-RARE-EPI for T_2 and T_2^* of MS patients, although the range of applications can be extended to several other brain pathologies as well as other target anatomy, disorders, and diseases. Recognizing the spin-physics of 2in1-RARE-EPI, this strategy can also be adapted to support simultaneous T_2 , T_2^* and temperature mapping.

ACKNOWLEDGMENTS

This project has received funding in part (T.N., T.W.E., J.M.M.) from the European Research Council (ERC) under the European Union's Horizon 2020 research and innovation program under grant agreement No 743077 (ThermalMR). The authors thank Eckart Grönerwaller and Beate Endemann (Berlin Ultrahigh Field Facility, Max-Delbrueck Center for Molecular Medicine in the Helmholtz Association) for supporting the study from a radiological perspective.

CONFLICT OF INTEREST

Thoralf Niendorf is founder and CEO of MRI.TOOLS, Berlin, Germany.


DATA AVAILABILITY STATEMENT


The data from this study are openly available at OSF: <https://www.osf.io/nf52q/>.

ORCID

Carl J. J. Herrmann  <https://orcid.org/0000-0002-5868-472X>

Laura Boehmert  <https://orcid.org/0000-0002-8703-3133>

Joao Periquito  <https://orcid.org/0000-0003-3702-9264>

Thomas Wilhelm Eigentler  <https://orcid.org/0000-0001-8252-450X>

Sonia Waiczies  <https://orcid.org/0000-0002-9916-9572>

REFERENCES

1. Filippi M, Bar-Or A, Piehl F, et al. Multiple sclerosis. *Nat Rev Dis Primers*. 2018;4:43.
2. Krieger SC, Cook K, De Nino S, Fletcher M. The topographical model of multiple sclerosis: a dynamic visualization of disease course. *Neurol Neuroimmunol Neuroinflamm*. 2016;3:e279.
3. Kutzelnigg A, Lucchinetti CF, Stadelmann C, et al. Cortical demyelination and diffuse white matter injury in multiple sclerosis. *Brain*. 2005;128:2705-2712.
4. Kuchling J, Paul F. Visualizing the central nervous system: imaging tools for multiple sclerosis and neuromyelitis optica spectrum disorders. *Front Neurol*. 2020;11:450.
5. Hemond CC, Bakshi R. Magnetic resonance imaging in multiple sclerosis. *Cold Spring Harb Perspect Med*. 2018;8:a028969.
6. Uher T, Schaedel S, Srpova B, et al. Monitoring of radiologic disease activity by serum neurofilaments in MS. *Neurol Neuroimmunol Neuroinflamm*. 2020;7:1-14.
7. Rust R, Chien C, Scheel M, et al. Epigallocatechin gallate in progressive MS: a randomized, placebo-controlled trial. *Neurol Neuroimmunol Neuroinflamm*. 2021;8:1-11.
8. Filippi M, Preziosa P, Meani A, et al. Prediction of a multiple sclerosis diagnosis in patients with clinically isolated syndrome using the 2016 MAGNIMS and 2010 McDonald criteria: a retrospective study. *Lancet Neurol*. 2018;17:133-142.
9. Inglese M, Petracca M. MRI in multiple sclerosis: clinical and research update. *Curr Opin Neurol*. 2018;31:249-255.
10. Filippi M, Preziosa P, Banwell BL, et al. Assessment of lesions on magnetic resonance imaging in multiple sclerosis: practical guidelines. *Brain*. 2019;142:1858-1875.
11. Karimian-Jazi K, Wildemann B, Diem R, et al. Gd contrast administration is dispensable in patients with MS without new T2 lesions on follow-up MRI. *Neurol Neuroimmunol Neuroinflamm*. 2018;5:1-7.
12. Filippi M, Preziosa P, Rocca MA. Chapter 20 - Multiple sclerosis. In: Masdeu J, González RG, eds. *Handbook of Clinical Neurology*, vol. 135. Amsterdam, Netherlands: Elsevier; 2016:399-423.
13. Geraldes R, Ciccarelli O, Barkhof F, et al. The current role of MRI in differentiating multiple sclerosis from its imaging mimics. *Nat Rev Neurol*. 2018;14:199.
14. Wuerfel J, Sinnecker T, Ringelstein EB, et al. Lesion morphology at 7 Tesla MRI differentiates Susac syndrome from multiple sclerosis. *Mult Scler*. 2012;18:1592-1599.
15. Sinnecker T, Dorr J, Pfueller CF, et al. Distinct lesion morphology at 7-T MRI differentiates neuromyelitis optica from multiple sclerosis. *Neurology*. 2012;79:708-714.
16. Sinnecker T, Clarke MA, Meier D, et al. Evaluation of the central vein sign as a diagnostic imaging biomarker in multiple sclerosis. *JAMA Neurology*. 2019;76:1446-1456.
17. Maranzano J, Dadar M, Rudko DA, et al. Comparison of multiple sclerosis cortical lesion types detected by multicontrast 3T and 7T MRI. *Am J Neuroradiol*. 2019;40:1162-1169.
18. Arevalo O, Riascos R, Rabiei P, Kamali A, Nelson F. Standardizing magnetic resonance imaging protocols, requisitions, and reports in multiple sclerosis: an update for radiologist based on 2017 magnetic resonance imaging in multiple sclerosis and 2018 consortium of multiple sclerosis centers consensus guidelines. *J Comput Assist Tomogr*. 2019;43:1-12.
19. Schmierer K, Champion T, Sinclair A, van Hecke W, Matthews PM, Wattjes MP. Towards a standard MRI protocol for multiple sclerosis across the UK. *Br J Radiol*. 2019;92:20180926.
20. Pereira DJ, Abreu P, Reis AM, et al. Consensus recommendations of the multiple sclerosis study group and the Portuguese neuroradiological society for the use of magnetic resonance imaging in multiple sclerosis in clinical practice: part 2. *Acta Médica Portuguesa*. 2020;33:66-75.
21. Saslow L, Li DKB, Halper J, et al. An international standardized magnetic resonance imaging protocol for diagnosis and follow-up of patients with multiple sclerosis: advocacy, dissemination, and implementation strategies. *Int J MS Care*. 2020;22:226-232.
22. Waiczies S, Els A, Kuchling J, et al. Magnetic resonance imaging of multiple sclerosis at 7.0 Tesla. *JoVE (Journal of Visualized Experiments)*. 2021;168:e62142.
23. Zivadinov R, Bakshi R. Role of MRI in multiple sclerosis I: inflammation and lesions. *Front Biosci*. 2004;9(665):C28.
24. Thompson AJ, Banwell BL, Barkhof F, et al. Diagnosis of multiple sclerosis: 2017 revisions of the McDonald criteria. *Lancet Neurol*. 2018;17:162-173.
25. Neema M, Stankiewicz J, Arora A, et al. T1-and T2-based MRI measures of diffuse gray matter and white matter damage in patients with multiple sclerosis. *J Neuroimaging*. 2007;17:16S-21S.
26. West J, Aalto A, Tisell A, et al. Normal appearing and diffusely abnormal white matter in patients with multiple sclerosis assessed with quantitative MR. *PLoS One*. 2014;9:1-9.
27. Neema M, Goldberg-Zimring D, Guss ZD, et al. 3 T MRI relaxation detects T2 prolongation in the cerebral normal-appearing white matter in multiple sclerosis. *NeuroImage*. 2009;46:633-641.
28. Reitz SC, Hof S-M, Fleischer V, et al. Multi-parametric quantitative MRI of normal appearing white matter in multiple sclerosis, and the effect of disease activity on T2. *Brain Imaging Behav*. 2017;11:744-753.
29. Whittall KP, MacKay AL, Li DK, Vavasour IM, Jones CK, Paty DW. Normal-appearing white matter in multiple sclerosis has heterogeneous, diffusely prolonged T2. *Magn Reson Med*. 2002;47:403-408.
30. Bonnier G, Roche A, Romascano D, et al. Advanced MRI unravels the nature of tissue alterations in early multiple sclerosis. *Ann Clin Transl Neurol*. 2014;1:423-432.
31. Uddin MN, Lebel RM, Seres P, Blevins G, Wilman AH. Spin echo transverse relaxation and atrophy in multiple sclerosis deep gray matter: a two-year longitudinal study. *Mult Scler J*. 2016;22:1133-1143.
32. McKenzie CA, Chen Z, Drost DJ, Prato FS. Fast acquisition of quantitative T2 maps. *Magn Reson Med*. 1999;41:208-212.
33. Sussman MS, Vidarsson L, Pauly JM, Cheng HLM. A technique for rapid single-echo spin-echo T2 mapping. *Magn Reson Med*. 2010;64:536-545.
34. Deoni SC, Peters TM, Rutt BK. High-resolution T1 and T2 mapping of the brain in a clinically acceptable time with DESPOT1 and DESPOT2. *Magn Reson Med*. 2005;53:237-241.
35. Ben-Eliezer N, Sodickson DK, Shepherd T, Wiggins GC, Block KT. Accelerated and motion-robust in vivo T2 mapping from radially undersampled data using bloch-simulation-based iterative reconstruction. *Magn Reson Med*. 2016;75:1346-1354.
36. Block KT, Uecker M, Frahm J. Model-based iterative reconstruction for radial fast spin-echo MRI. *IEEE Trans Med Imaging*. 2009;28:1759-1769.
37. Sumpf TJ, Uecker M, Boretius S, Frahm J. Model-based nonlinear inverse reconstruction for T2 mapping using highly undersampled spin-echo MRI. *J Magn Reson Imaging*. 2011;34:420-428.

38. Tallantyre EC, Morgan PS, Dixon JE, et al. A comparison of 3T and 7T in the detection of small parenchymal veins within MS lesions. *Invest Radiol.* 2009;44:491-494.
39. Sinnecker T, Schumacher S, Mueller K, et al. MRI phase changes in multiple sclerosis vs neuromyelitis optica lesions at 7T. *Neurol Neuroimmunol Neuroinflamm.* 2016;3:e259.
40. Bagnato F, Hametner S, Boyd E, et al. Untangling the R2* contrast in multiple sclerosis: a combined MRI-histology study at 7.0 Tesla. *PLoS One.* 2018;13:1-19.
41. Walsh AJ, Lebel RM, Eissa A, et al. Multiple sclerosis: validation of MR imaging for quantification and detection of iron. *Radiology.* 2013;267:531-542.
42. Bozin I, Ge Y, Kuchling J, et al. Magnetic resonance phase alterations in multiple sclerosis patients with short and long disease duration. *PLoS One.* 2015;10:e0128386.
43. Ropele S, Kilsdonk ID, Wattjes MP, et al. Determinants of iron accumulation in deep grey matter of multiple sclerosis patients. *Mult Scler J.* 2014;20:1692-1698.
44. Walsh AJ, Blevins G, Lebel RM, Seres P, Emery DJ, Wilman AH. Longitudinal MR imaging of iron in multiple sclerosis: an imaging marker of disease. *Radiology.* 2014;270:186-196.
45. Blazejewska AI, Al-Radaideh AM, Wharton S, et al. Increase in the iron content of the substantia nigra and red nucleus in multiple sclerosis and clinically isolated syndrome: a 7 Tesla MRI study. *J Magn Reson Imaging.* 2015;41:1065-1070.
46. Zhang Y, Gauthier SA, Gupta A, et al. Magnetic susceptibility from quantitative susceptibility mapping can differentiate new enhancing from nonenhancing multiple sclerosis lesions without gadolinium injection. *Am J Neuroradiol.* 2016;37:1794-1799.
47. Schlemm L, Chien C, Bellmann-Strobl J, et al. Gadopentetate but not gadobutrol accumulates in the dentate nucleus of multiple sclerosis patients. *Mult Scler J.* 2017;23:963-972.
48. El-Khatib AH, Radbruch H, Trog S, et al. Gadolinium in human brain sections and colocalization with other elements. *Neurol Neuroimmunol Neuroinflamm.* 2019;6:1-3.
49. Cox EF, Gowland PA. Simultaneous quantification of T2 and T'2 using a combined gradient echo-spin echo sequence at ultrahigh field. *Magn Reson Med.* 2010;64:1440-1445.
50. Donahue KM, Van Kylen J, Guven S, et al. Simultaneous gradient-echo/spin-echo EPI of graded ischemia in human skeletal muscle. *J Magn Reson Imaging.* 1998;8:1106-1113.
51. Remmele S, Ring J, S enegas J, et al. Concurrent MR blood volume and vessel size estimation in tumors by robust and simultaneous $\Delta R2$ and $\Delta R2^*$ quantification. *Magn Reson Med.* 2011;66:144-153.
52. Thomas DL, Lythgoe MF, Gadian DG, Ordidge RJ. Rapid simultaneous mapping of T2 and T2* by multiple acquisition of spin and gradient echoes using interleaved echo planar imaging (MASAGE-IEPI). *Neuroimage.* 2002;15:992-1002.
53. van de Maat G, de Leeuw H, Seevinck P, van den Bosch M, Nijssen J, Bakker C. Simultaneous R2*, R2, and R2' quantification by combining S0 estimation of the free induction decay with a single spin echo: a single acquisition method for R2 insensitive quantification of holmium-166-loaded microspheres. *Magn Reson Med.* 2015;73:273-283.
54. Wang C, Zhang R, Zhang X, et al. Simultaneous dynamic R2, and measurement using periodic π pulse shifting multiecho asymmetric spin echo sequence moving estimation strategy: a feasibility study for lower extremity muscle. *Magn Reson Med.* 2017;77:766-773.
55. Wang Y, Zhang R, Zhang B, et al. Simultaneous R2, R2' and R2* measurement of skeletal muscle in a rabbit model of unilateral artery embolization. *Magn Reson Imaging.* 2019;61:149-157.
56. Balasubramanian M, Polimeni JR, Mulkern RV. In vivo measurements of irreversible and reversible transverse relaxation rates in human basal ganglia at 7 T: making inferences about the microscopic and mesoscopic structure of iron and calcification deposits. *NMR Biomed.* 2019;32:e4140.
57. Yablonskiy DA, Haacke EM. An MRI method for measuring T2 in the presence of static and RF magnetic field inhomogeneities. *Magn Reson Med.* 1997;37:872-876.
58. Li N, Bolding M, Twieg DB. Spin-echo SS-PARSE: a PARSE MRI method to estimate frequency, R2 and R2' in a single shot. *Magn Reson Imaging.* 2010;28:1270-1282.
59. Schmiedeskamp H, Straka M, Newbould RD, et al. Combined spin- and gradient-echo perfusion-weighted imaging. *Magn Reson Med.* 2012;68:30-40.
60. Jin N, Guo Y, Zhang Z, Zhang L, Lu G, Larson AC. GESFIDE-PROPELLER approach for simultaneous R2 and R2* measurements in the abdomen. *Magn Reson Imaging.* 2013;31:1760-1765.
61. Hillenbrand C, Hahn D, Haase A, Jakob P. MR CAT scan: a modular approach for hybrid imaging. *MAGMA.* 2000;10:183-199.
62. Fuchs K, Hezel F, Klix S, Mecke R, Wuerfel J, Niendorf T. Simultaneous dual contrast weighting using double echo rapid acquisition with relaxation enhancement (RARE) imaging. *Magn Reson Med.* 2014;72:1590-1598.
63. Paul K, Huelnhagen T, Oberacker E, et al. Multiband diffusion-weighted MRI of the eye and orbit free of geometric distortions using a RARE-EPI hybrid. *NMR Biomed.* 2018;31:1-18.
64. Theilmann RJ, Gmitro AF, Altbach MI, Trouard TP. View-ordering in radial fast spin-echo imaging. *Magn Reson Med.* 2004;51:768-774.
65. Sedlacik J, Boelmans K, L obel U, Holst B, Siemonsen S, Fiehler J. Reversible, irreversible and effective transverse relaxation rates in normal aging brain at 3 T. *Neuroimage.* 2014;84:1032-1041.
66. Stanisz GJ, Odrobina EE, Pun J, et al. T1, T2 relaxation and magnetization transfer in tissue at 3T. *Magn Reson Med.* 2005;54:507-512.
67. Wansapura JP, Holland SK, Dunn RS, Ball WS Jr. NMR relaxation times in the human brain at 3.0 tesla. *Magn Reson Med.* 1999;9:531-538.
68. Peters AM, Brookes MJ, Hoogenraad FG, et al. T2* measurements in human brain at 1.5, 3 and 7 T. *Magn Reson Imaging.* 2007;25:748-753.
69. Block KT, Uecker M. Simple method for adaptive gradient-delay compensation in radial MRI. In Proceedings of the 19th Annual Meeting of ISMRM, Montr el, CA, 2011, p. 2816.
70. Fessler J, Sutton B, Zhang Y. *Michigan Image Reconstruction Toolbox*. Ann Arbor, MI: Jeffrey Fessler. <https://web.eecs.umich.edu/~fessler/code/>
71. Lustig M. *SparseMRI V0.2*, Berkeley, CA: Michael Lustig. https://people.eecs.berkeley.edu/~mlustig/software/sparseMRI_v0.2
72. Lustig M, Donoho D, Pauly JM. Sparse MRI: the application of compressed sensing for rapid MR imaging. *Magn Reson Med.* 2007;58:1182-1195.
73. Lustig M, Donoho DL, Santos JM, Pauly JM. Compressed sensing MRI. *IEEE Signal Process Mag.* 2008;25:72-82.
74. Lebel RM, Wilman AH. Transverse relaxometry with stimulated echo compensation. *Magn Reson Med.* 2010;64:1005-1014.

75. Winkelmann S, Schaeffter T, Weiss S, Eggers H, Doessel O. Simultaneous imaging and R2* mapping using a radial multi-gradient-echo (rMGE) sequence. *J Magn Reson Imaging*. 2006;24:939-944.
76. Rohrer M, Bauer H, Mintorovitch J, Requardt M, Weinmann H-J. Comparison of magnetic properties of MRI contrast media solutions at different magnetic field strengths. *Invest Radiol*. 2005;40:715-724.
77. Weerakoon BS, Osuga T, Konishi T. Enhancement effect of superparamagnetic iron oxide nanoparticle-based MRI contrast agent at different concentrations and magnetic field strengths. *Int J Miner Metall Mater*. 2016;10:50-53.
78. Dahnke H, Schaeffter T. Limits of detection of SPIO at 3.0 T using T2* relaxometry. *Magn Reson Med*. 2005;53:1202-1206.
79. Whittall KP, Mackay AL, Graeb DA, Nugent RA, Li DK, Paty DW. In vivo measurement of T2 distributions and water contents in normal human brain. *Magn Reson Med*. 1997;37:34-43.
80. Laule C, Vavasour IM, Kolind SH, et al. Magnetic resonance imaging of myelin. *Neurotherapeutics*. 2007;4:460-484.
81. Kitzler HH, Wahl H, Eisele JC, et al. Multi-component relaxation in clinically isolated syndrome: lesion myelination may predict multiple sclerosis conversion. *Neuroimage Clin*. 2018;20:61-70.
82. Norris DG, Koopmans PJ, Boyacioglu R, Barth M. Power independent of number of slices (PINS) radiofrequency pulses for low-power simultaneous multislice excitation. *Magn Reson Med*. 2011;66:1234-1240.
83. Norris DG, Boyacioglu R, Schulz J, Barth M, Koopmans PJ. Application of PINS radiofrequency pulses to reduce power deposition in RARE/turbo spin echo imaging of the human head. *Magn Reson Med*. 2014;71:44-49.
84. Gagoski BA, Bilgic B, Eichner C, et al. RARE/turbo spin echo imaging with simultaneous multislice wave-CAIPI. *Magn Reson Med*. 2015;73:929-938.
85. Hennig J, Scheffler K. Hyperechoes. *Magn Reson Med*. 2001;46:6-12.
86. Hennig J, Weigel M, Scheffler K. Multiecho sequences with variable refocusing flip angles: optimization of signal behavior using smooth transitions between pseudo steady states (TRAPS). *Magn Reson Med*. 2003;49:527-535.
87. Filippi M, Preziosa P, Rocca MA. MRI in multiple sclerosis: what is changing? *Curr Opin Neurol*. 2018;31:386-395.
88. Millward JM, Ramos Delgado P, Smorodchenko A, et al. Transient enlargement of brain ventricles during relapsing-remitting multiple sclerosis and experimental autoimmune encephalomyelitis JCI. *Insight*. 2020;5:21.
89. Azevedo CJ, Cen SY, Jaberzadeh A, Zheng L, Hauser SL, Pelletier D. Contribution of normal aging to brain atrophy in MS. *Neurol Neuroimmunol Neuroinflamm*. 2019;6:e616.
90. Pawlitzki M, Horbrügger M, Loewe K, et al. MS optic neuritis-induced long-term structural changes within the visual pathway. *Neurol Neuroimmunol Neuroinflamm*. 2020;7:1-9.
91. Wang C, Barnett MH, Yiannikas C, et al. Lesion activity and chronic demyelination are the major determinants of brain atrophy in MS. *Neurol Neuroimmunol Neuroinflamm*. 2019;6:e593.
92. Kuchling J, Brandt AU, Paul F, Scheel M. Diffusion tensor imaging for multilevel assessment of the visual pathway: possibilities for personalized outcome prediction in autoimmune disorders of the central nervous system. *EPMA Journal*. 2017;8:279-294.
93. Waiczies H, Lepore S, Drechsler S, et al. Visualizing brain inflammation with a shingled-leg radio-frequency head probe for 19F/1H MRI. *Sci Rep*. 2013;3:1280.
94. Lepore S, Waiczies H, Hentschel J, et al. Enlargement of cerebral ventricles as an early indicator of encephalomyelitis. *PLoS One*. 2013;8:e72841.
95. Donadieu M, Kelly H, Szczupak D, et al. Ultrahigh-resolution MRI reveals extensive cortical demyelination in a nonhuman primate model of multiple sclerosis. *Cereb Cortex*. 2020;31:439-447.
96. Johnston G, Johnson T, Solomon AJ, et al. Limited utility of gadolinium contrast administration in routine multiple sclerosis surveillance. *J Neuroimaging*. 2020;31:103-107.
97. Sadigh G, Saindane AM, Waldman AD, Lava NS, Hu R. Comparison of unenhanced and gadolinium-enhanced imaging in multiple sclerosis: is contrast needed for routine follow-up MRI? *Am J Neuroradiol*. 2019;40:1476-1480.
98. Gupta A, Al-Dasuqi K, Xia F, et al. The use of noncontrast quantitative MRI to detect gadolinium-enhancing multiple sclerosis brain lesions: a systematic review and meta-analysis. *Am J Neuroradiol*. 2017;38:1317-1322.
99. Mittal S, Wu Z, Neelavalli J, Haacke EM. Susceptibility-weighted imaging: technical aspects and clinical applications, part 2. *Am J Neuroradiol*. 2009;30:232-252.
100. Haacke EM, Mittal S, Wu Z, Neelavalli J, Cheng YC. Susceptibility-weighted imaging: technical aspects and clinical applications, part 1. *Am J Neuroradiol*. 2009;30:19-30.
101. Jang J, Nam Y, Choi Y, et al. Paramagnetic rims in multiple sclerosis and neuromyelitis optica spectrum disorder: a quantitative susceptibility mapping study with 3-T MRI. *J Clin Neurol*. 2020;16:562-572.
102. Huelnhagen T, Ku M-C, Reimann HM, et al. Myocardial effective transverse relaxation time T2(*) is elevated in hypertrophic cardiomyopathy: a 7.0 T magnetic resonance imaging study. *Sci Rep*. 2018;8:3974.
103. Huelnhagen T, Hezel F, Serradas Duarte T, et al. Myocardial effective transverse relaxation time T2* Correlates with left ventricular wall thickness: A 7.0 T MRI study. *Magn Reson Med*. 2017;77:2381-2389.
104. van den Boomen M, Manhard MK, Snel GJH, et al. Blood oxygen level-dependent MRI of the myocardium with multiecho gradient-echo spin-echo imaging. *Radiology*. 2020;294:538-545.
105. Niendorf T, Pohlmann A, Arakelyan K, et al. How bold is blood oxygenation level-dependent (BOLD) magnetic resonance imaging of the kidney? Opportunities, challenges and future directions. *Acta Physiol (Oxf)*. 2015;213:19-38.
106. Caroli A, Pruijm M, Burnier M, Selby NM. Functional magnetic resonance imaging of the kidneys: where do we stand? The perspective of the European COST action PARENCHIMA. *Nephrol Dial Transplant*. 2018;33(suppl_2):ii1-ii3.
107. Caroli A, Remuzzi A, Remuzzi G. Does MRI trump pathology? A new era for staging and monitoring of kidney fibrosis. *Kidney Int*. 2020;97:442-444.
108. Muir ER, Pan X, Donaldson PJ, et al. Multi-parametric MRI of the physiology and optics of the in-vivo mouse lens. *Magn Reson Imaging*. 2020;70:145-154.
109. Tonev D, Shumbayawonda E, Tetlow LA, et al. The effect of multi-parametric magnetic resonance imaging in standard of care for nonalcoholic fatty liver disease: protocol for a randomized control trial. *JMIR Research Protocols*. 2020;9:e19189.
110. Lindner T, Langner S, Falke K, et al. Anatomic and pathological characterization of choroidal melanoma using multimodal imaging: what is practical, what is needed? *Melanoma Res*. 2015;25:252-258.

111. Butts K, de Crespigny A, Pauly JM, Moseley M. Diffusion-weighted interleaved echo-planar imaging with a pair of orthogonal navigator echoes. *Magn Reson Med.* 1996;35:763-770.
112. Atkinson D, Porter DA, Hill DL, Calamante F, Connelly A. Sampling and reconstruction effects due to motion in diffusion-weighted interleaved echo planar imaging. *Magn Reson Med.* 2000;44:101-109.

How to cite this article: Herrmann CJJ, Els A, Boehmert L, et al. Simultaneous T_2 and T_2^* mapping of multiple sclerosis lesions with radial RARE-EPI. *Magn Reson Med.* 2021;86:1383–1402. <https://doi.org/10.1002/mrm.28811>